

BOSTON UNIVERSITY
GRADUATE SCHOOL OF ARTS AND SCIENCES

Dissertation

**MEASUREMENT OF THE MAGNETIC ANOMALY OF
THE MUON TO X PARTS PER BILLION IN RUN 1 OF
THE FERMILAB MUON $g - 2$ EXPERIMENT**

by

NICHOLAS BRENNAN KINNAIRD

B.S., University of Texas at Austin, 2013
B.S., University of Texas at Austin, 2013
M.A., Boston University, 2016

Submitted in partial fulfillment of the
requirements for the degree of
Doctor of Philosophy

2019

© 2019 by
NICHOLAS BRENNAN KINNAIRD
All rights reserved

Approved by

First Reader

B. L. Roberts, PhD
Professor of Physics

Second Reader

R. M. Carey, PhD
Professor of Physics

Dedication

I dedicate this thesis to

Acknowledgments

Here go all your acknowledgments. You know, your advisor, funding agency, lab mates, etc., and of course your family.

As for me, I would like to thank Jonathan Polimeni for cleaning up old LaTeX style files and templates so that Engineering students would not have to suffer typesetting dissertations in MS Word. Also, I would like to thank IDS/ISS group (ECE) and CV/CNS lab graduates for their contributions and tweaks to this scheme over the years (after many frustrations when preparing their final document for BU library). In particular, I would like to thank Limor Martin who has helped with the transition to PDF-only dissertation format (no more printing hardcopies – hooray !!!)

The stylistic and aesthetic conventions implemented in this LaTeX thesis/dissertation format would not have been possible without the help from Brendan McDermot of Mugar library and Martha Wellman of CAS.

Finally, credit is due to Stephen Gildea for the MIT style file off which this current version is based, and Paolo Gaudiano for porting the MIT style to one compatible with BU requirements.

Janusz Konrad
Professor
ECE Department

**MEASUREMENT OF THE MAGNETIC ANOMALY OF
THE MUON TO X PARTS PER BILLION IN RUN 1 OF
THE FERMILAB MUON $g - 2$ EXPERIMENT**

(Order No.)

NICHOLAS BRENNAN KINNAIRD

Boston University, Graduate School of Arts and Sciences, 2019

Major Professor: B. L. Roberts, Professor of Physics

ABSTRACT

This abstract was copied from my departmental seminar, and it needs to be updated for my thesis: One of the few indications for new physics is the discrepancy between the theoretical and experimental values for the anomalous magnetic moment of the muon. There is a 3 to 4 sigma discrepancy between theory and the last experimental measurement held at Brookhaven National Laboratory in 2001, which measured the muon g-2 to 540 parts per billion. This discrepancy has been consistent for many years now with ever improving theoretical calculations and other experimental measurements. In order to resolve or confirm this difference, a new experiment is underway at Fermilab to measure the muon g-2 to 4 times higher precision at 140 ppb. Muon g-2 at Fermilab gathered its first production data in 2018, and is currently taking data now. I will describe the principles of the experiment and detail two specific parts of the analysis that I have been involved in. These include track fitting and precession frequency analysis of the Run 1 data.

Contents

1	Introduction	1
1.1	Magnetic moments of particles	2
1.2	Standard Model contributions to a_μ	3
1.2.1	QED	4
1.2.2	Electroweak	5
1.2.3	Hadronic	6
1.2.4	Combined Standard Model value	8
1.3	Experimental value of a_μ and discrepancy with a_μ^{SM}	9
1.4	Beyond the Standard Model and the purpose of E989	11
2	Principle Techniques of E989	14
2.1	Measuring ω_a	16
2.2	Measuring the magnetic field	20
2.3	Production of polarized muons	25
2.4	Injection of muons	28
2.5	Storage of muons	31
2.5.1	Kicker	31
2.5.2	Electrostatic quadrupoles	32
2.6	Muon beam dynamics	34
2.6.1	Coherent betatron oscillation	37
2.6.2	Beam debunching	38
2.7	Corrections to ω_a	41

2.7.1	Electric field correction	41
2.7.2	Pitch correction	43
2.8	Run 1 in E989	45
3	Detector Systems	48
3.1	Auxiliary detectors	48
3.1.1	T0	48
3.1.2	Inflector Beam Monitoring System	49
3.1.3	Fiber harps	50
3.2	Calorimeters	52
3.2.1	Requirements and systematic effects	52
3.2.2	Hardware	53
3.2.3	Laser calibration system	56
3.3	Straw trackers	56
3.3.1	Tracker readout electronics	62
4	Track Reconstruction and Analysis	64
4.1	Track Finding	64
4.2	Track Fitting	67
4.2.1	Geometry and error propagation	67
4.2.2	χ^2 minimization	74
4.2.3	Left right ambiguity	79
4.3	Track Extrapolation	79
4.4	Muon Beam Measurements	80
5	ω_a Measurement	86
5.1	Details of Run 1	86
5.2	Reconstruction	86
5.2.1	Clustering	86

5.3	Histogramming	86
5.4	Fitting	86
5.5	Systematic Errors	86
6	Conclusion	87
6.1	Run 1 value of a_μ	87
A	g for Spin-1/2 Particles	88
B	Ratio Method Derivation	91
B.1	Ratio form and function	91
B.2	Ratio errors	96
C	Pileup Modified Errors	97
C.1	Pileup errors for the ratio function	100

List of Tables

2.1	Uncertainties in the magnetic field measurement	25
2.2	Muon beam frequencies in the E989 experiment	36
2.3	Run 1 datasets	47
C.1	Number of doublet counts added to pileup histogram from shadow method	98

List of Figures

1.1	QED diagrams contributing to the magnetic moment	4
1.2	Electroweak diagrams contributing to the magnetic moment	5
1.3	First order hadronic vacuum polarization diagram contributing to the magnetic moment	7
1.4	Hadronic light-by-light diagrams contributing to the magnetic moment	9
1.5	Comparison between theoretical and experimental values for a_μ . . .	10
1.6	General diagram for new physics	12
1.7	Citations for E821 publications vs year	13
2.1	Feynman diagrams for muon and pion decay	17
2.2	Muon decay pictures for maximum and minimum energy decay positrons	17
2.3	Number distribution and asymmetry for muon decay in the muon rest frame and lab frame	18
2.4	$g - 2$ wiggle example	20
2.5	Magnet cross section	22
2.6	FID signal	23
2.7	Azimuthally averaged magnetic field sample	24
2.8	Fermilab accelerator layout for muon delivery to E989	26
2.9	Fermilab accelerator pulse train	27
2.10	Muon injection point through inflector	29
2.11	Superconducting inflector magnet	30
2.12	The $g - 2$ experiment	30

2.13	Vacuum chamber map	32
2.14	Electrostatic quadrupoles installed in a vacuum chamber	33
2.15	Electrostatic quadrupole potentials	34
2.16	Tune plane	37
2.17	Coherent betatron oscillation	39
2.18	Beam debunching fast rotation	40
2.19	Pitching beam motion	43
3.1	T0 counter and pulses	49
3.2	IBMS Models	50
3.3	IBMS Positions	50
3.4	Fiber harp and measurement	51
3.5	Calorimeters	54
3.6	SiPM pulse	55
3.7	Straw tracker drift circles	58
3.8	Tracker module	59
3.9	Tracker module coordinate system	60
3.10	TrackerCaloWithLines	61
3.11	Tracker electronics readout chain	63
4.1	Track candidate selection	66
4.2	Vertical and radial magnetic fields calculated in Opera2D	69
4.3	Tracker reference frame	71
4.4	Fitting matrices diagram	79
4.5	Geane code flow	80
4.6	Birds eye view of extrapolation in ring	81
4.7	Extrapolated muon beam distribution cross-section	82
4.8	CBO frequency	83

4.9 CBO amplitude	84
-----------------------------	----

List of Abbreviations

ASDQ	Amplifier Shaper Discriminator with charge (Q)
ASIC	application specific integrated circuit
BNL	Brookhaven National Laboratory
BSM	beyond the standard model
CBO	coherent betatron oscillation
E821	Brookhaven Muon $g - 2$ Experiment
E989	Fermilab Muon $g - 2$ Experiment
EW	electroweak
FID	free-induction decay
FNAL	Fermi National Accelerator Laboratory
Geane	Geometry and Error Propagation
Geant4	Geometry and Tracking 4
IBMS	inflector beam monitoring system
NMR	nuclear magnetic resonance
PCB	printed circuitry board
PMT	photo-multiplier tube
POT	protons on target
ppb	parts per billion
ppm	parts per million
QCD	quantum chromodynamics
QED	quantum electrodynamics
RMS	root mean square
SiPM	silicon photo-multiplier
SM	Standard Model
STDP	short-term double pulse
VW	vertical waist
WFD	waveform digitizer

Chapter 1

Introduction

The prevailing theory for particle physics, the Standard Model (SM), has had tremendous success in describing our universe. It has been used to predict and explain a wide variety of phenomena, particles, properties, and interactions to great precision. However, in spite of its success in explaining nearly all experimental results, there remain unanswered questions about our universe. Some of these include the matter-antimatter asymmetry, the source of mass for the neutrinos, the existence of dark matter, and an inability to fully incorporate our best theory of gravitation. Many particle physics experiments around the world are being devised and conducted in order to shed light on these questions and improve our understanding of reality. One such particular experiment is the Fermilab Muon $g - 2$ Experiment (E989) underway at the Fermi National Accelerator Laboratory (FNAL) located in Batavia, Illinois.

I have been a part of the E989 experiment since I began my graduate degree six years ago. Three years ago I moved from Boston to Batavia to get more involved by being where the action is. This dissertation will describe the E989 experiment and the work which I have done for it along the way in detail. Chapter 1 will provide experimental and theoretical background to the experiment, as well its motivation. Chapter 2 will describe the experimental principle and specifics to muon production and storage. Chapter 3 will describe the various detector systems. Chapter 4 will describe the straw tracking reconstruction including the track fitting algorithm I wrote, as well as some analysis results. Chapter 5 will describe the precession frequency

measurement portion of the experiment, and detail my analysis results from data taken in the first half of 2018. Chapter 6 will conclude the thesis and the results contained within.

1.1 Magnetic moments of particles

In order to understand the purpose of the Fermilab Muon $g - 2$ Experiment, first we need to understand what the g in $g - 2$ is. This is what the experiment is measuring. All particles have intrinsic properties. One property of charged particles is the magnetic dipole moment.¹ This property of a particle is related to its spin through the equation

$$\vec{\mu} = g \frac{q}{2m} \vec{s}, \quad (1.1)$$

where $\vec{\mu}$ is the magnetic dipole moment of a particle, \vec{s} is its spin vector, m is its mass, $q = \pm e$ where e is the elementary charge, and g is the so called "g-factor". g is some measurable and predictable constant, which as shown in Equation 1.1 relates the magnetic moment of a particle to its spin angular momentum. Since the torque on a particle in a magnetic field is

$$\vec{N} = \vec{\mu} \times \vec{B}, \quad (1.2)$$

the rate at which a particles spin precesses in a magnetic field will depend on g . This happens to be one of the key physics principles in the E989 experiment as will be discussed later.

In a Dirac theory, g is equal to 2 for spin-1/2 particles with no internal structure [1]. See Appendix A for a nice derivation of this result. It turns out however, that g is not quite equal to 2 even for these types of particles. Motivated by early experimental

¹*Magnetic dipole moment* and *magnetic moment* are equivalent when talking about particles.

discrepancies such as the measurements of the hyperfine structure in hydrogen [2], in 1948 Schwinger calculated the first "radiative correction" to the electron magnetic moment [3]. In a quantum field theory, interactions of the particle with virtual particles in loops will contribute to the value of g . In this context it is nicer to recast the magnetic dipole moment formula as

$$\vec{\mu} = 2(1 + a) \frac{q}{2m} \vec{s},$$

$$a = \frac{g - 2}{2}, \quad (1.3)$$

where a is called the "anomalous" part of the magnetic moment, and contains all higher order corrections. The first correction calculated to a by Schwinger was $a = \alpha/2\pi \approx 0.00116$, where α is the fine structure constant. By measuring a , the SM theory can be tested and extensions to it constrained. The measurement of the anomalous piece of the muon is indeed where the Fermilab Muon $g - 2$ Experiment gets its name.

1.2 Standard Model contributions to a_μ

Before experimental results have any real meaning, they need a theory with which to compare. The latest theoretical predictions for the muon magnetic moment will be presented here. The contributions to a_μ can be summed from separate pieces relating to different parts of the SM. These include the quantum-electrodynamics (QED) corrections purely from other leptons and photons, the electroweak (EW) corrections from interactions with the weak force bosons W^\pm and Z^0 , and the hadronic corrections from interactions with hadrons:

$$a_\mu^{\text{SM}} = a_\mu^{\text{QED}} + a_\mu^{\text{EW}} + a_\mu^{\text{Had}} \quad (1.4)$$

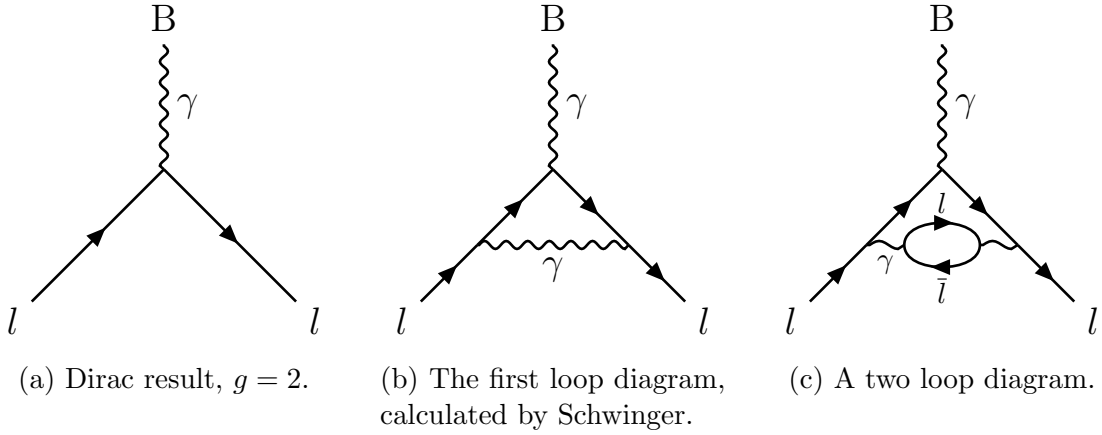


Figure 1.1: The first of many QED diagrams contributing to a . B is an external magnetic field. Feynman diagrams made with References [4, 5].

1.2.1 QED

The QED contributions to a_μ stem solely from loops with virtual leptons and photons. They are very well understood and have been calculated to very high order, having been calculated up to five loop level from over 12,000 Feynman diagrams [6, 7]. This has been done either analytically or numerically. The first couple of diagrams including the Dirac $g = 2$ and Schwinger diagrams are shown in Figure 1.1. The value is

$$a_\mu^{\text{QED}} = \sum_{n=1}^{\infty} C_n \left(\frac{\alpha}{\pi} \right)^n, \quad (1.5)$$

$$= (11658471.8971 \pm 0.0007) \times 10^{-10},$$

where in the first line a_μ^{QED} is expressed as a perturbative expansion in the fine structure constant. $C_1 = 1/2$ is the Schwinger result mentioned previously stemming from the diagram shown in Figure 1.1b. Over 99% of the value of a_μ comes from the QED sector, but the error is much smaller than the other contributions, as well as the experimental uncertainty.

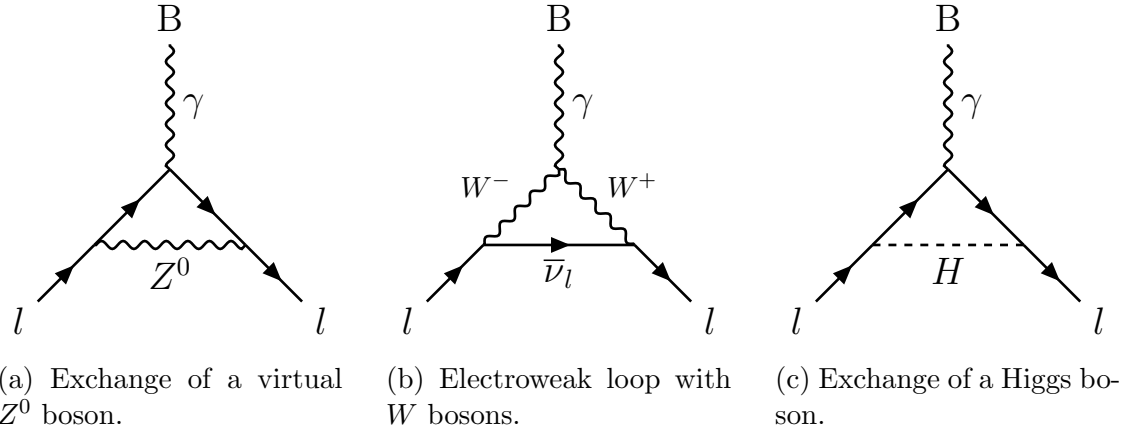


Figure 1.2: First order weak diagrams contributing to a_μ . B is an external magnetic field. Feynman diagrams made with References [4, 5].

1.2.2 Electroweak

The electroweak contributions to a_μ are known to two loop level, with some three loop parts estimated. The contributions stem from couplings with the heavy weak gauge bosons. The different one loop diagrams are shown in Figure 1.2. Per usual Feynman rules, the propagators will contain the masses of the interacting bosons, while the kinematics will contain the masses of the leptons. For calculations of a muon in the case of Figure 1.2a, these result in a factor $\sim (m_\mu/m_{Z^0})^2$. Because the mass of the gauge bosons are so much more than the muon, these processes are necessarily suppressed and the electroweak contributions to a_μ are small. For this reason knowing these contributions only up to two loop level is sufficient. The value of the electroweak contributions is

$$a_\mu^{\text{EW}} = (15.12 \pm 0.01) \times 10^{-10}, \quad (1.6)$$

with improvements having been made recently [8, 9]. Again the error on these contributions is small compared to the hadronic contributions discussed next, as well as the experimental uncertainty.

1.2.3 Hadronic

The hadronic contributions to a_μ stem from interactions with virtual hadrons. Because they cannot be calculated perturbatively at low energies due to the QCD nature of these particles, these calculations comprise the dominant uncertainty in the SM calculation. This makes their error estimation extra important when comparing to experiment. Most active work on the theoretical side of things is in this sector. These contributions can be separated into two parts

$$a_\mu^{\text{Had}} = a_\mu^{\text{HVP}} + a_\mu^{\text{HLbL}}. \quad (1.7)$$

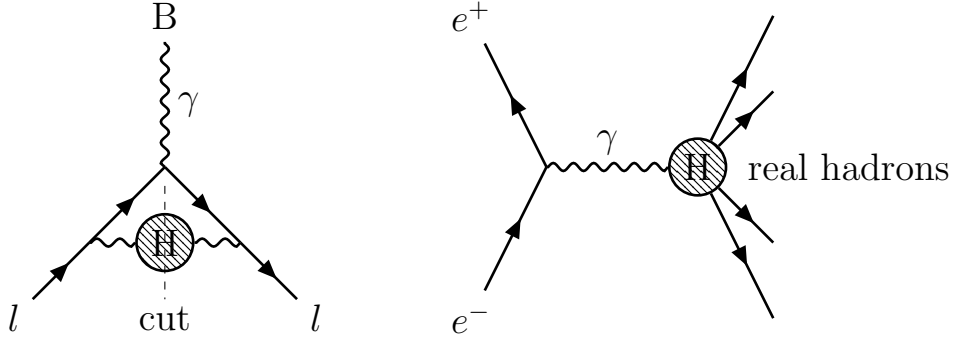
Hadronic Vacuum Polarization

The first of these hadronic contribution parts is the hadronic vacuum polarization part (HVP), the first order diagram of which is shown in Figure 1.3a. There are two main prescriptions for calculating these contributions. The first is to use a dispersive approach to introduce a virtual hadron blob into the integral calculation for the photon propagator [10], and then utilize the optical theorem to relate the imaginary part of that propagator to the total cross-section of electron-positron annihilation to hadrons. While this could be solved perturbatively for a lepton blob in place of the hadron blob, this is instead a data driven approach when considering non-perturbative QCD. The details of dispersion theory will not be described here. The leading order contribution can be written as

$$a_\mu^{\text{HVP;LO}} = \left(\frac{\alpha m_\mu}{3\pi} \right)^2 \int_{m_\pi^2}^{\infty} \frac{ds}{s^2} K(s) R(s) \quad (1.8)$$

where $K(s)$ is some kinematic factor, and $R(s)$ is a ratio of cross-sections

$$R(s) = \frac{\sigma(e^+e^- \rightarrow \text{hadrons})}{\sigma(e^+e^- \rightarrow \mu^+\mu^-)}. \quad (1.9)$$



(a) The first order HVP diagram. The blob H in the middle indicates any combination of hadrons which satisfy the Feynman rules.

(b) The Feynman diagram for electron positron annihilation to hadrons.

Figure 1.3: The first order HVP diagram on the left, which can be related to the diagram on the right by making a 'cut' across the virtual hadrons blob. B is an external magnetic field. Feynman diagrams made with References [4, 5].

The cross-section data for this relation has been measured in parts by various experiments, including KLOE, CLEO, BaBar, and BESIII [11, 12, 13, 14]. The analysis by Keshavarzi et al. [15] gives results as

$$\begin{aligned} a_\mu^{\text{HVP;LO}} &= (693.26 \pm 2.46) \times 10^{-10}, \\ a_\mu^{\text{HVP;NLO}} &= (-9.82 \pm 0.04) \times 10^{-10}, \end{aligned} \quad (1.10)$$

where $a_\mu^{\text{HVP;NLO}}$ is the next to leading order calculation. This evaluation is consistent with Davier et al. [16]. In this way, the SM theory has some dependence on experimental results. This is acceptable as the experimental measurements are straightforward observables.

The second prescription to estimating the HVP contributions is a first principles approach, using lattice QCD and QED. It is a gauge theory defined on a matrix of points in time and space. Once the matrix is taken infinitely large with the spacing between the points infinitely small, the behavior from a continuous theory is recov-

ered. The results for the leading order estimates of $a_\mu^{\text{HVP;LO}}$ are consistent with those provided above, though the error is larger. If the calculation is supplemented with the cross-section data described above, then this method provides the most precise determination of $a_\mu^{\text{HVP;LO}}$ [17].

Hadronic Light-by-Light

The second of these hadronic contribution parts is a higher order four photon interaction, termed hadronic light-by-light. Diagrams are shown in Figure 1.4. Again perturbation theory is unable to assist in the calculation of these contributions. For a long time the calculation of these diagrams was model dependent, and has therefore been the most contentious part of the SM calculation. In more recent years, there have been efforts to produce results using dispersive [18, 19, 20] and lattice approaches [21, 22, 23]. A cumulative report on recent progress is given by N. Asmussen et al. [24]. The error on this contribution is large due to these various approaches, comparable to that of the $a_\mu^{\text{HVP;LO}}$ term, even though the size of this contribution is small. The value of the HLbL contributions to a_μ quoted by Keshavarzi et al. and given by Nyffeler [15, 25] comes from model estimates and is

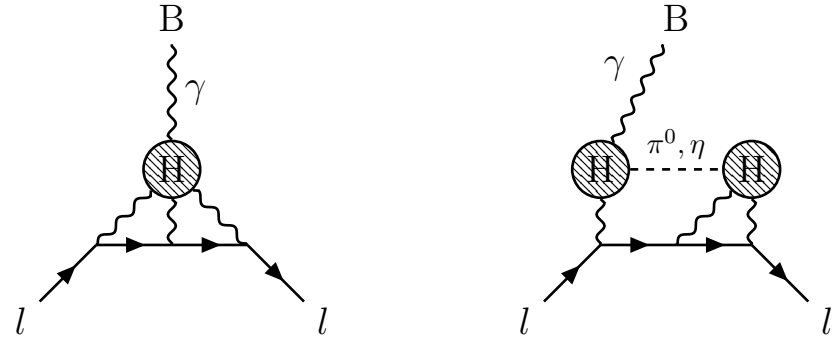
$$a_\mu^{\text{HLbL}} = (9.8 \pm 2.6) \times 10^{-10}. \quad (1.11)$$

1.2.4 Combined Standard Model value

The sum of the a_μ contributions listed here is

$$\begin{aligned} a_\mu^{\text{SM}} &= a_\mu^{\text{QED}} + a_\mu^{\text{EW}} + a_\mu^{\text{Had}}, \\ &= (11659180.26 \pm 3.58) \times 10^{-10}. \end{aligned} \quad (1.12)$$

The relative uncertainty of this result is 307 ppb. Other analyses with different values for the various contributions typically agree well, as shown on the left side of



(a) The first HLbL diagram, where three photons are exchanged with some virtual hadrons blob.

(b) A second HLbL diagram, where three photons are exchanged with two virtual hadrons blobs, that are connected with some virtual chargeless propagator.

Figure 1.4: HLbL diagrams contributing to a_μ . B is an external magnetic field. Feynman diagrams made with References [4, 5].

Figure 1.5. Depending on what calculations are used, the discrepancy between theory and experiment ranges between 3 to 4 standard deviations. The latest experimental result is described in the following section.

1.3 Experimental value of a_μ and discrepancy with a_μ^{SM}

The theoretical contributions to a_μ listed in the previous sections have improved over time as methods have matured and more experimental data gathered. Similarly, work on the direct experimental measurement of a_μ has been going on for decades, with more precise results being determined over time [26]. The most recent experiment to measure $g-2$ was the Brookhaven Muon $g-2$ Experiment (E821) held at Brookhaven National Laboratory (BNL) in 2001 [27]. That experiment measured a value for a_μ of

$$a_\mu^{\text{Exp}} = (11659208.0 \pm 6.3) \times 10^{-10}, \quad (1.13)$$

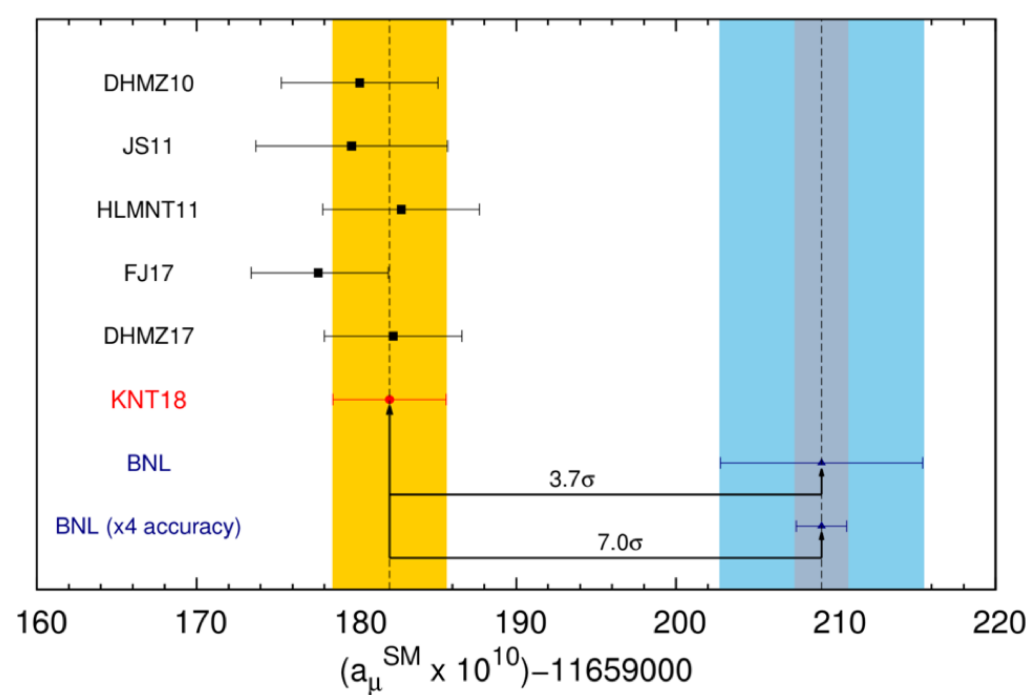


Figure 1.5: Various theoretical values for a_μ on the left, as compared to the most recent and extrapolated experimental result on the right. Plot courtesy of Alex Keshavarzi [15].

which corresponds to a 540 ppb relative uncertainty. Note that the uncertainty of the experimental measurement is comparable to that of the theory, necessitating precise understanding of all the different theoretical parts. The difference between the experimental and theoretical values here is

$$a_\mu^{\text{Exp}} - a_\mu^{\text{SM}} = (27.74 \pm 7.25) \times 10^{-10}, \quad (1.14)$$

corresponding to a discrepancy of 3.83σ from 0.

1.4 Beyond the Standard Model and the purpose of E989

While the discrepancy between experiment and theory might be attributed to miscalculations in the theory or systematic errors in the E821 experiment, no such errors have been found despite serious attempts to resolve the two. Indeed the discrepancy has only grown over time as the theoretical calculations have matured. The most intriguing and exciting source of the discrepancy would be physics beyond the standard model (BSM). Since the value of a_μ receives contributions from all particles that couple to the muon through virtual loops, unknown particles might be the source of this discrepancy. Specifically, since the contribution to the magnetic moment from heavy virtual particles goes as

$$a \sim \frac{m^2}{\Lambda^2}, \quad (1.15)$$

where Λ is the mass scale of the new particle and m the mass of the lepton in question, the sensitivity of the muon as compared to the electron to large mass scales is $m_\mu^2/m_e^2 \approx 43,000$ times greater. It is possible from this reason that even though the magnetic moment of the electron has been measured extraordinarily precisely, to .23 ppb [28, 29], it has provided no indication of anything new, whereas the magnetic moment of the muon might provide definitive evidence of new physics. (As a brief side

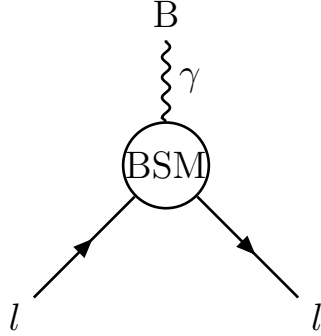


Figure 1.6: A general Feynman diagram, where the leptons couple to an external magnetic field B through some BSM physics. Feynman diagrams made with References [4, 5].

note, a recent measurement of the fine structure constant α to the highest precision yet [30] has yielded a new value of a_e for which the difference between theory and experiment is 2.5 standard deviations, but with the opposite sign as compared to a_μ .)

A basic example diagram of new physics is shown in Figure 1.6. Because the discrepancy from the previous experiment was not at the 5 standard deviation level necessary to classify it as a discovery, the E989 experiment was undertaken. Indeed with the lack of new physics results coming out of the LHC and other experiments, E989 is especially positioned to uncover something new at a time where there are so few hints of new physics. Because of this, the interest in the E821 experiment and underway E989 experiment has only grown over time. The number of citations for the E821 results has been consistently high over the years and is shown in Figure 1.7.

The E989 experiment has the goal of measuring a_μ to 140 ppb over the course of several years. This would be a factor of 4 improvement over the E821 result stemming from a 20 times increase in statistics, which was the limiter in the previous experiment. Assuming the same value for a_μ is obtained, this would push the statistical significance of the discrepancy over the 5 standard deviation mark to approximately 7 standard deviations, as shown in Figure 1.5. The data comprising Run 1, gathered in the spring and summer of 2018, is the subject of this thesis, and corresponds to an experimental

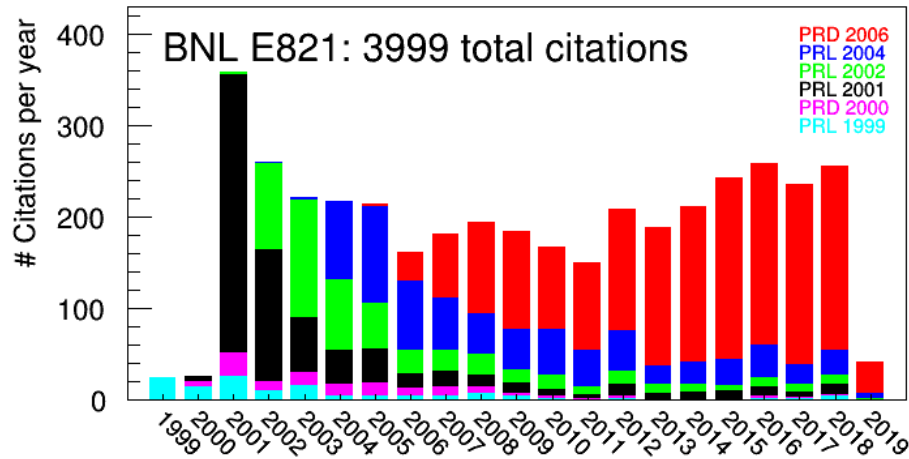


Figure 1.7: The number of citations for the BNL experiment publications as a function of year. Plot courtesy of Mark Lancaster. **Update this plot before submission.**

uncertainty comparable to the E821 result. When it's all said and done, the possibility is that we will measure something new and exciting. Even if we do not however, it is valuable in itself to resolve this theoretical and experimental conflict.

Chapter 2

Principle Techniques of E989

As referenced in Equation 1.2, a particle in a magnetic field will experience a torque which attempts to line up the magnetic dipole moment of the particle with the external field. Because of this, in a dipole field a particles spin will turn at the precession frequency [31]

$$\vec{\omega}_s = -g \frac{q}{2m} \vec{B} - (1 - \gamma) \frac{q}{\gamma m} \vec{B}, \quad (2.1)$$

where as before m is the particles mass, $q = \pm e$ where e is the positive elementary charge, g is the g-factor, γ is the Lorentz relativistic factor, and B is an external magnetic field. The first term is the usual Larmor frequency and the second term is a relativistic correction to the precession frequency called Thomas precession [31]. Similarly, a particle with some momentum will orbit at the cyclotron frequency

$$\vec{\omega}_c = -\frac{q}{\gamma m} \vec{B}. \quad (2.2)$$

By taking the difference between these two frequencies we arrive at the “spin difference frequency”

$$\vec{\omega}_a = \vec{\omega}_s - \vec{\omega}_c = -\frac{g - 2}{2} \frac{q}{m} \vec{B} = -a \frac{q}{m} \vec{B}, \quad (2.3)$$

a frequency that is directly proportional to anomaly a . If $g = 2$ as in a Dirac theory, then the particles spin would turn at the same rate as the momentum vector, and

this spin difference frequency ω_a would be identically zero. If this spin difference frequency for a muon and the external magnetic dipole field can be measured, then the anomalous magnetic moment of the muon a_μ can be measured.

As will be detailed below in Section 2.2, the measurement of the magnetic field is related to the Larmor precession frequency of free protons in water

$$\omega_p = -g_p \frac{e}{2m_p} B, \quad (2.4)$$

where g_p and m_p are the g-factor and mass of the proton respectively. Replacing B and solving for a_μ , we arrive at

$$a_\mu = \frac{g_p}{2} \frac{\omega_a}{\omega_p} \frac{m_\mu}{m_p}. \quad (2.5)$$

Using the magnetic moment formulas for the proton, electron, and muon as shown in Equation 1.1, Equation 2.5 can be transformed to either of the following consistent equations:

$$\begin{aligned} a_\mu &= \frac{g_e}{2} \frac{\omega_a}{\omega_p} \frac{m_\mu}{m_e} \frac{\mu_p}{\mu_e} \\ a_\mu &= \frac{\omega_a/\omega_p}{\lambda - \omega_a/\omega_p} \end{aligned} \quad (2.6)$$

Here the p , e , and μ subscripts stand for the relevant quantities for the proton, electron, and muon respectively. In the second equation $\lambda = \mu_\mu/\mu_p$. As mentioned before the electron g-factor g_e has been measured to extremely high precision, 0.26 ppt [28, 29]. The muon-electron mass ratio m_μ/m_e and muon-proton magnetic moment ratio λ have been measured to 22 ppb [29, 32]. Finally the proton-electron magnetic moment ratio μ_p/μ_e has been measured to 3 ppb [29]. The errors on these terms are small compared to the target uncertainty for E989 of 140 ppb, the measurement of which now comes down to measuring the ratio ω_a/ω_p .

2.1 Measuring ω_a

How can ω_a for muons be measured? The answer lies with two key points in the dynamics of muon decay. Positive muons decay to a positron and two neutrinos, as shown in Figure 2.1a. The first point is that because of the parity violating nature of the weak interaction, the decay positron will be preferentially emitted right-handed, with its spin directed in the same direction as its momentum [33]. The second key point is that angular momentum must be conserved. Consider the most extreme examples of maximum and minimum energy positrons as shown in Figure 2.2. In the muon rest frame, decay positrons with maximum energy will be emitted opposite to the two neutrinos. Since neutrinos and anti-neutrinos must be left and right-handed respectively, thus having their spins anti-parallel and parallel to their momentum, by the law of conservation of angular momentum the positron must have its spin be parallel to the spin of the muon at the time of the decay. By the opposite argument, decay positrons emitted with minimum energy such that the neutrinos are ejected opposite to one another must have their spins be anti-parallel to that of the muon at the time of decay. These two points combined together means that higher energy decay positrons will preferentially be emitted in directions parallel to the muon spin at the time of decay, while lower energy decay positrons will preferentially be emitted in directions anti-parallel to the muon spin at the time of the decay.

This correlation between the emitted direction of the decay positron and the spin of the muon is the signature needed to measure ω_a . By placing an ensemble of polarized muons within a magnetic storage ring, those muons will orbit at the cyclotron frequency and their spins will precess at the Larmor frequency. As they go around the ring they will decay to positrons whose energy and decay directions contain information about the spin of the muon. The differential decay distribution



Figure 2·1: Feynman diagrams for muon (left) and pion (right) decay.

Muon decay in the rest frame



Figure 2·2: Muon decay pictures for maximum and minimum energy decay positrons. Due to the conservation of angular momentum and the single possible helicity states of the decay neutrinos, the spin of the decay positron is exactly parallel to the spin of the muon at the time of the decay for maximum energy decay positrons (top), or anti-parallel for minimum energy decay positrons (bottom).

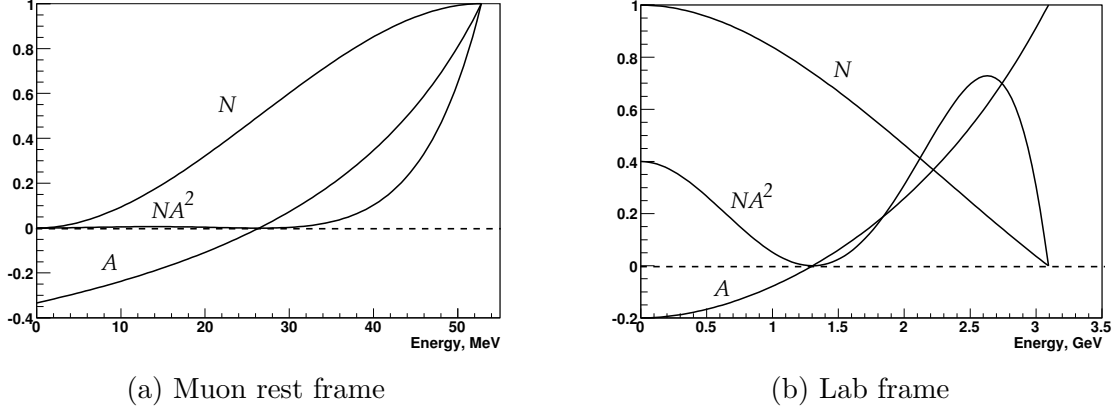


Figure 2.3: Decay number distribution N and asymmetry A in the muon rest frame (left) and in the lab frame (right) as a function of positron energy with a maximum positron energy of 3.1 GeV.

in the muon rest frame is described by [33]

$$dP(y, \theta) \propto N(y)[1 \pm A(y) \cos(\theta)]dyd\Omega, \quad (2.7)$$

where $y = E/E_{max}$ is the energy fraction of the positron, θ is the angle between the spin of the muon and the momentum of the positron $\cos^{-1}(\hat{p} \cdot \hat{s})$, and the \pm stands for the positive and negative muon respectively. $N(y)$ is the number distribution of decay positrons and $A(y)$ is the so called 'asymmetry' encoding the preferred positron decay direction. Here the energy of the positron is assumed to be much greater than its mass. The number distribution and asymmetry are given by [33]

$$N(y) = 2y^2(3 - 2y^2), \quad (2.8)$$

$$A(y) = \frac{2y - 1}{3 - 2y}, \quad (2.9)$$

and are shown in Figure 2.3a.

In the lab frame for high energy positrons, nearly all positrons will be emitted parallel to the muon momentum, which makes it challenging to select purely on the decay angle of the positron. That's not a problem though, as we already know that

decay positrons with higher energies will be emitted in directions parallel to the muon spin at the time of decay. Essentially, the energy distribution of detected positrons for high energies is modulated by ω_a , or $\theta = \omega_a t + \phi$. The number of detected positrons at some time and energy in the lab frame for some initial number N_0 of muons can then be described by

$$N_d(t, E) = N_0(E) \cdot e^{-t/\gamma\tau_\mu} \cdot [1 + A(E) \cos(\omega_a t + \phi(E))], \quad (2.10)$$

where the d subscript stands for 'detected,' the muons are decaying at a lifetime of $\gamma\tau_\mu$, and all the relevant parameters are energy dependent. Here $N_0(E)$ and $A(E)$ have been transformed from Equations 2.8 and 2.9 to the lab frame,

$$N_0(E) \propto (y - 1)(4y^2 - 5y - 5), \quad (2.11)$$

$$A(E) = \frac{-8y^2 + y + 1}{4y^2 - 5y - 5}, \quad (2.12)$$

where as a reminder $y = E/E_{max}$. Here the polarization of the muons is assumed to be unity. These are shown in Figure 2.3b. To increase the amount of statistics, all positrons above some energy threshold cut E_{th} can be taken as the observable,

$$N_d(t, E_{th}) = N_0(E_{th}) \cdot e^{-t/\gamma\tau_\mu} \cdot [1 + A(E_{th}) \cos(\omega_a t + \phi(E_{th}))], \quad (2.13)$$

where the number and asymmetry of the detected positrons is now calculated by simply integrating Equations 2.11 and 2.12 from y_{th} to 1,

$$N_0(E_{th}) \propto (y_{th} - 1)^2(-y_{th}^2 + y_{th} + 3), \quad (2.14)$$

$$A(E_{th}) = \frac{y_{th}(2y_{th} + 1)}{-y_{th}^2 + y_{th} + 3}, \quad (2.15)$$

where $y_{th} = E_{th}/E_{max}$. By fitting Equation 2.13, ω_a can be extracted. An sample of data adhering to Equation 2.13 is shown in Figure 2.4.

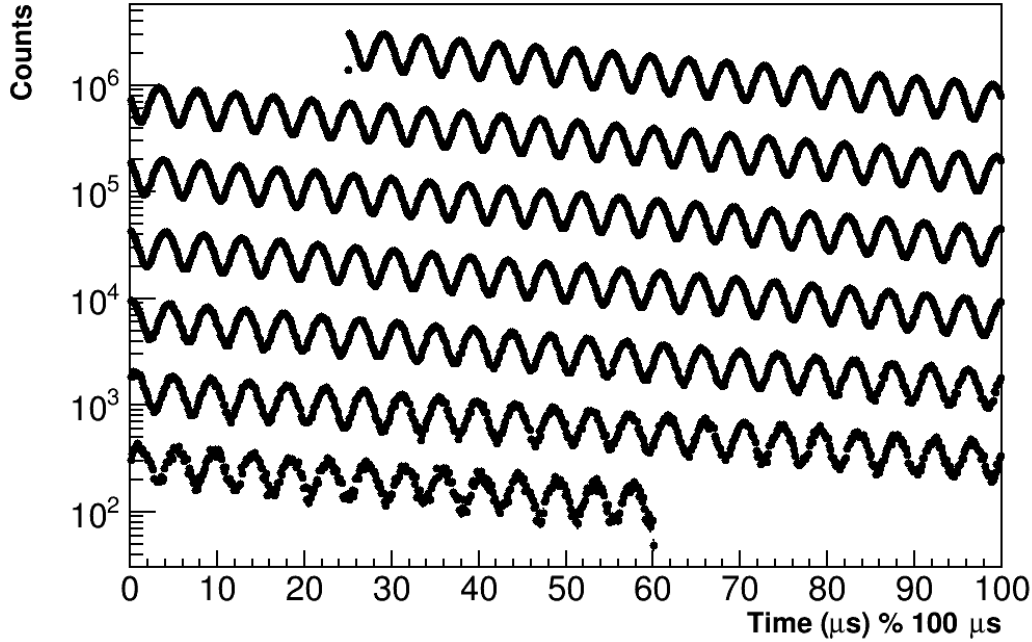


Figure 2.4: The number of detected positrons above some energy threshold ($y \sim 0.55$) as a function of time. The time axis is wrapped around every $100\text{ }\mu\text{s}$.

2.2 Measuring the magnetic field

In order to measure the magnetic moment of the muon to 140 ppb, the field needs to be both highly uniform, and measured to extreme precision. The E989 goal for the field measurement is 70 ppb. As shown in Equation 2.6 the measurement of the magnetic field has equal weight to that of the precession frequency. A cross-section of the magnetic ring is shown in Figure 2.5. The muons live within a 9 cm^2 diameter cylindrical storage region at the center of the magnetic field. This corresponds to an approximately 0.28 m^3 or 10 ft^3 total volume around the inside of the ring. The magnetic field is made uniform by manipulating many magnetic ‘knobs’ built into the $g - 2$ storage ring, including the main magnet current, pole pieces, wedges, top hats, and thousands of small magnetic shims placed around the storage region. There is also an active feedback system which stabilizes the magnetic field over time. The shimming

of the field to high precision, to an RMS (root mean square) of approximately 25 ppm, was a long process of fine tuning over the course of many months that was undertaken by many members of the field team.

Measuring the magnetic field comes down to measuring ω_p as shown in Equation 2.4. This is because the magnetic field measurement is made using a pulsed nuclear magnetic resonance technique (NMR). NMR was chosen as it provides a field measurement precision on the order of 10 ppb with negligible statistical uncertainty [34]. NMR probes work by rotating the magnetization of a sample of protons in some fluid, typically water or petroleum jelly, and then measuring the relaxation time or free-induction decay (FID) signal of the proton spins. The magnetization of the protons will relax back to equilibrium with the external field as the spins of the protons precess at the Larmor frequency and interact with local magnetic field gradients or inhomogeneities. Pickup coils are located around the sample which both deliver the pulse to rotate the proton sample magnetization and measure the FID signal. An example of an FID signal is shown in Figure 2.6.

Technically, it is not solely ω_p that needs to be measured. What really matters is the average magnetic field that the muons see, or the time-averaged spatially-weighted magnetic field. The scheme devised to measure this is two-fold. First, the magnetic field in the storage region where the muons live is measured by a trolley which drives around the inside of the ring. This trolley holds 17 NMR probes and measures the field at approximately 6000 locations around the inside of the ring. Because however the trolley cannot be in the beam path when the muons are present in the ring, during data taking it is pulled out of the way and the field is instead measured by 378 fixed NMR probes located in the high magnetic field region, but just outside the storage region. The prescription is that the fixed probes measure the field at all times, the storage ring field is measured every few days by the trolley probes, and the two



g-2 Magnet in Cross Section

Figure 2-5: Cross-section of the $g - 2$ magnet. The muons live in the storage region. This is surrounded by many magnetic features of the magnet which allow for sub ppm level tuning of the magnetic field.

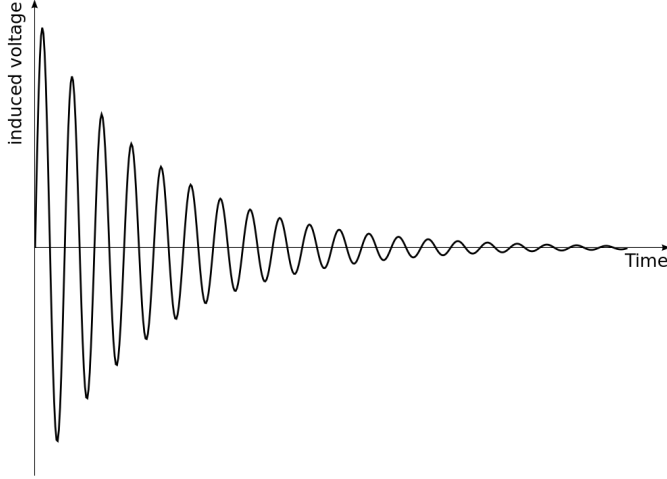


Figure 2.6: An example FID signal. The current picked up in the coils around the proton sample will oscillate as the spins precess around the main magnetic field, and decay as the spins return to alignment with the external field.

are interpolated. In this way the magnetic field can be mapped over time and over the space that the muons live in. A preliminary sample of the azimuthally-averaged magnetic field measured with trolley and fixed probes is shown in Figure 2.7.

Lastly, it is the free proton precession frequency in the field that is of interest, but the frequency that the probes measure will be different due to the molecular properties of the proton sample as well as the material properties of the probe itself. The frequency that the probes measure can be re-casted as

$$\omega_{p,\text{probe}} = \omega_{p,\text{free}}(1 - \sigma(\text{H}_2\text{O}, T) + \delta_b + \delta_p + \delta_s), \quad (2.16)$$

where $\sigma(\text{H}_2\text{O}, T)$ is the temperature dependent diamagnetic shielding of protons in a water molecule, and the δ 's come from corrections due to the bulk susceptibility of the water sample, paramagnetic impurities in the water sample, and the magnetic effects of the probe itself, respectively [34]. In order to correct for these effects two additional special probes are used, both of which live in a single section of the ring which has

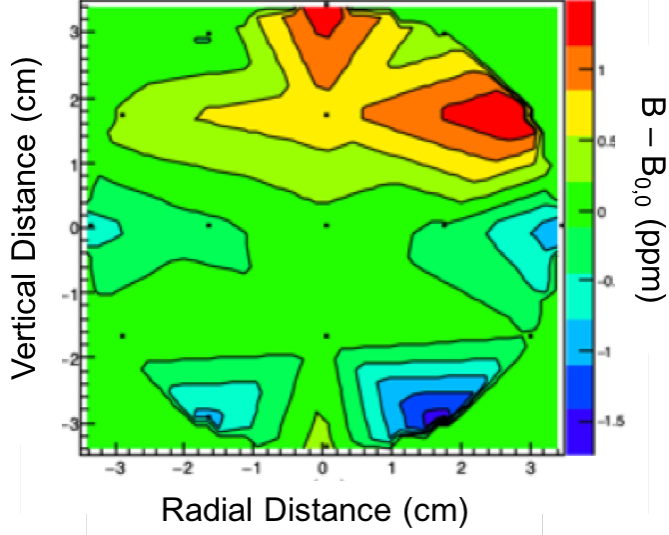


Figure 2·7: A sample of the azimuthally-averaged magnetic field within the storage region. The contours are normalized to the center value of the field. The scale of the field differences is approximately ± 1 ppm. The dots in the picture correspond to the location of the trolley probes. **Update this picture later on and find out what the time averaging is.**

been shimmed to extra uniformity. The first is a calibration probe which measures the free proton precession frequency at the center of the storage region corresponding to the placement of the central trolley probe. The calibration probe is made of materials in order to reduce the effects in Equation 2.16 and has been characterized in other test magnets. The second special probe is called the ‘plunging probe.’ This probe lives inside the vacuum chamber and drops into the storage region to measure the field at each of the 17 trolley probe locations, using a three dimensional motion system. By using these two probes, the calibration for the free proton precession frequency can be transmitted to each of the trolley probes, providing for the needed measurement inside the storage region of the magnetic field. This calibration procedure is estimated to take up about half of the target systematic uncertainty of 70 ppb at 35 ppb.

Other pieces of the systematic uncertainty include the absolute calibration of the

Magnetic Field Measurement Uncertainties	
Source of uncertainty	E989 Goal (ppb)
Absolute calibration of standard probe	35
Calibration of trolley probes	30
Trolley measurements	30
Fixed probe interpolation	30
Muon distribution weighted average	10
Time dependent external fields	5
Others	30
Quadrature sum	70

Table 2.1: Systematic errors in the magnetic field measurement. Unlisted sources of error include the measurement of higher field multipoles, trolley temperature and power supply voltage response effects, and eddy currents from the kicker, among others.

calibration probe, the trolley measurements, the interpolation to the fixed probes, the uncertainty relative to the muon distribution, and others such as time dependent external magnetic fields. See Table 2.1 When all is said and done, the measurement of the magnetic field is a complex and continuous process that is done in parallel to the measurement of ω_a throughout data taking.

2.3 Production of polarized muons

As explained previously, the number of high energy positrons detected depends on the muon spin at the time of decay. In order for this detected quantity to mean anything, the muon spins themselves need to be highly polarized. Using the same parity-violation and spin momentum conservation logic as expounded upon in muon decay, it is determined that pion decay produces muons that are 100% polarized in the pion rest frame, due to the pion having zero spin. The Feynman diagram for this decay is shown in Figure 2.1b. It's also important to note that pions decay to muons with over 99% branching ratio due to the parity violating nature of the weak

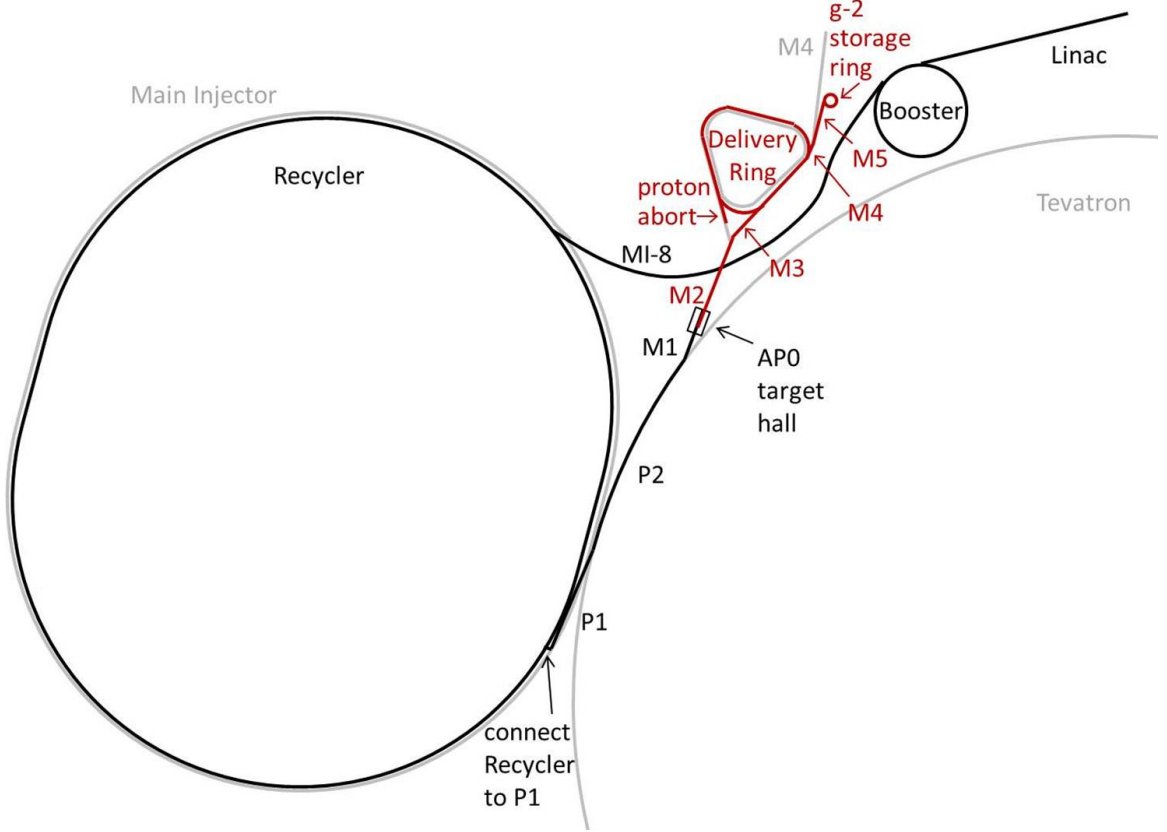


Figure 2.8: Plotted is the layout of accelerator beam-line components Fermilab uses to provide polarized muons to E989. Protons start in the Linac, traverse around the Booster and then Recycler, and are converted to pions at AP0. The pions are gathered and then decay away to muons in the Delivery Ring before being sent to the $g - 2$ storage ring. Figure taken from Reference [34].

interaction, and thus a preference for the heavier muon over the electron. These two facets of pion decay are used to construct polarized muon beams.

In order to measure $g - 2$ to high precision, a very large number of positrons need to be detected, and hence a large number of highly polarized muons injected into the storage ring. The BNL E821 experiment observed on the order of 10 billion positrons above threshold, and its final result was statistics limited. In order to reach the goal of 140 ppb, 20 times that number of statistics needs to be gathered. The only facility in the world that can produce such a high number of polarized muons is Fermilab.



Figure 2.9: General timing structure of beam pulses sent to E989.

The Fermilab accelerator complex produces polarized muons for E989 in a number of stages. A map of the various relevant accelerator beam-line components is shown in Figure 2.8. Details of the full accelerator production of polarized muons can be found in Reference [35], and here will be given a summary of the process. First, protons are generated and accelerated in a linear accelerator. They are transported to a small circular ring called the “booster,” which accelerates them up to 8 GeV and batches them together. A single booster batch contains on the order of 4×10^{12} protons. The protons are then injected into a ring called “recycler,” which re-bunches them into four separate bunches of 1×10^{12} protons, each with a time width of approximately 120 ns. (This is less than the cyclotron period of the storage ring of 149 ns.) This rebunching process is done in order to reduce the level of pileup in the $g - 2$ detectors, see Section 3.2.1. For a single accelerator supercycle of 1.4 s, E989 receives four booster batches of particles corresponding to sixteen bunches at an average rate of 11.4 Hz, with the time separation between bunches greater than 10 ms. The timing structure is shown in Figure 2.9. The sets of eight bunches are sometimes referred to as pulses, and the gathered data is tagged by which bunch or pulse it originates from. Depending on the accelerator requirements of other experiments, this timing structure is modified appropriately though it is relatively constant.

Each bunch is selected one at a time and sent to a target hall, where the bunch is directed on to an Inconel target. This Inconel target is made up of a nickel and

iron alloy optimized for producing a large number of pions with a small momentum spread, approximately $1 \times 10^{-5} \pi^+/\text{POT}$ with $|dp/p| < 2\%$ [35]. The resulting pions are focused just after production by a lithium lens. This lithium lens is a 1 cm radius and 15 cm long piece of lithium designed to carry high current which provides a radial focusing effect for particles passing lengthwise down the cylinder [36]. A pulsed magnet just after the lithium lens is then used to select pions at 3.115 GeV.

In a pion beam the highest and lowest energy decay muons are polarized. The pion beam and any residual protons or secondaries are injected into another ring called the “delivery ring”. By the time the pions have gotten to the delivery ring, most of them have decayed to muons. The delivery ring is used to both hold the beam until the remaining pions decay, which takes about four turns, and to select the polarized muons [35]. Forward emitted polarized muons are momentum selected at 3.094 GeV with $\Delta p/p = 2\%$. The remaining muons, protons, and other secondary particles are separated and re-routed to a beam dump which reduces the contamination in the final polarized muon beam. This polarized muon beam is then sent to the $g - 2$ building where it passes through four magnetic quadrupole focusing magnets before being injected into the storage ring.

2.4 Injection of muons

The injection of the muon beam into the $g - 2$ storage ring is a specialized process. In order to measure the magnetic field to the precision described in Section 2.2, the $g - 2$ storage ring must be a single monolithic magnet with no end effects. This prohibits the usual design of separated magnetic elements through which the muons might be injected. Therefore we use a specialized magnet called the “Superconducting Inflector” magnet, or just inflector. This inflector is placed just after a bored out tunnel in the storage ring magnet, on the inside of the C shape. See Figure 2.10 for a

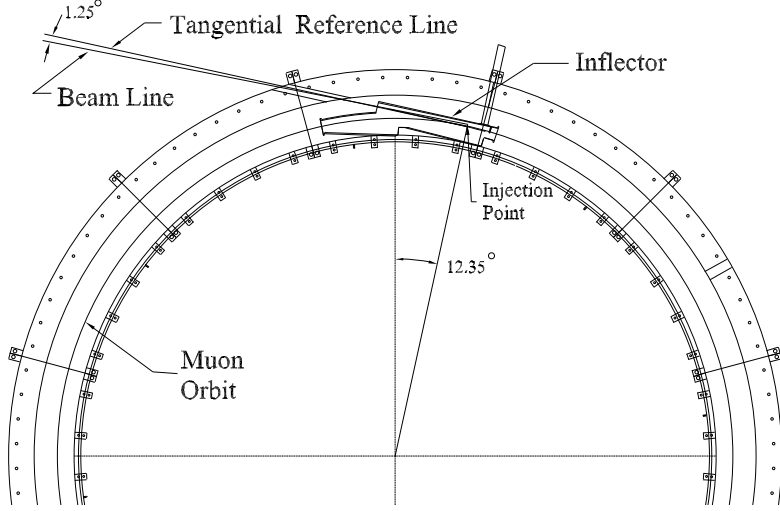


Figure 2·10: Shown is a plan view of the inflector and injection point into the storage ring [37].

view of the injection point. The inflector has a very tight 18 mm wide by 56 mm high aperture through which the muons must pass down its 1.7 m length. The inflector is made up of superconducting coils wrapped in a double cosine theta design around an aluminum mandrel [37]. See Figure 2·11. This design serves to contain the majority of the inflector magnet field, while eliminating the the storage ring field for the muons passing down its length, such that they are not lost due to motion induced by said field. The inflector is contained within a superconducting shield which traps the fringe field of the inflector such that the storage ring magnet field is unaffected. As shown in Figure 2·11, both sides of the inflector are closed such that an appreciable fraction of muons are lost due to multiple scattering before being injected into the ring. Approximately 2% of injected muons are stored with $\Delta p/p = 0.1\%$ centered around 3.094 GeV. A new inflector magnet is being designed with open ends in order to increase the muon flux for future runs of $g - 2$ [34].

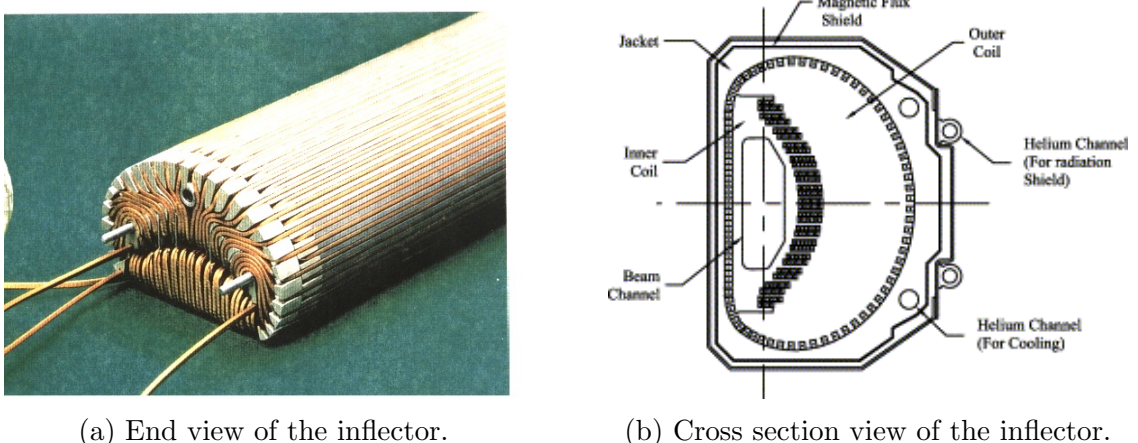


Figure 2.11: The inflector magnet (left) and a cross section view of the inflector windings and associated shield (right) [37].

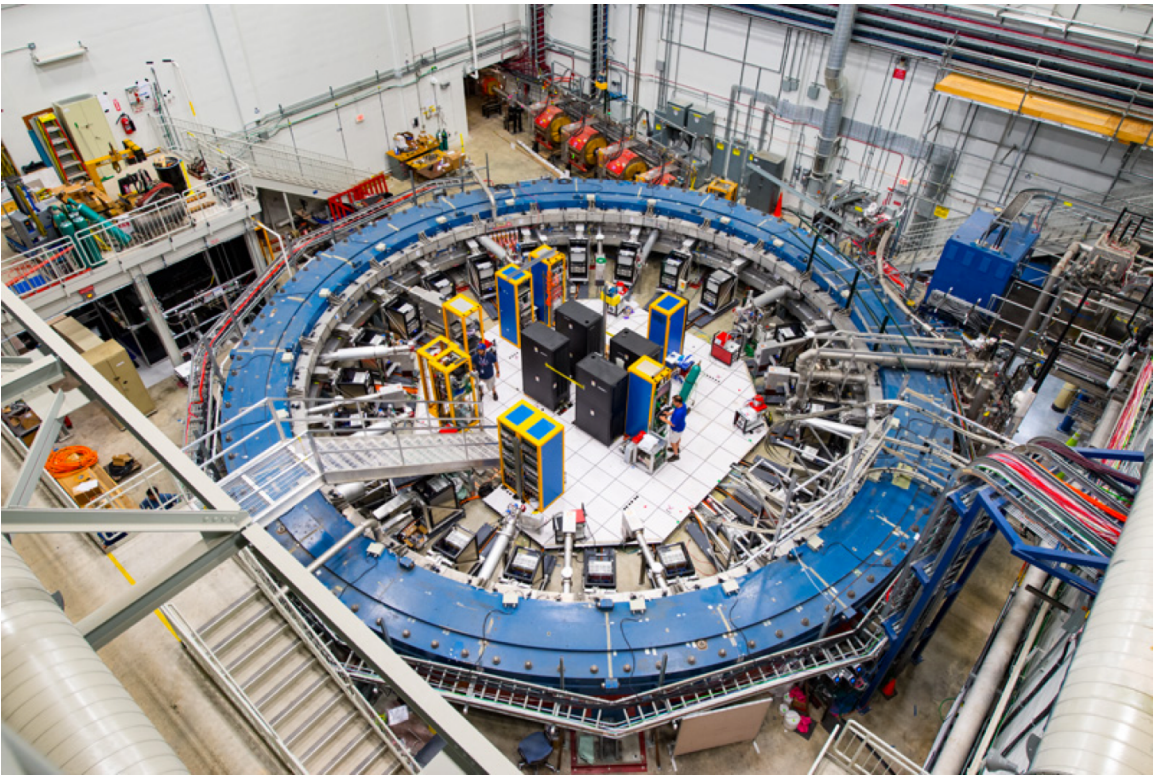


Figure 2.12: Shown is a picture of the $g - 2$ experiment. The blue painted storage ring can be seen to surround a variety of detectors and electronics. Muons come in at the top of the picture through a series of magnetic quadrupoles from the accelerator and are injected into the ring, where they orbit in a clockwise direction. There are some people located inside the ring which gives a sense of scale to the picture.

2.5 Storage of muons

The E989 experiment and storage ring are shown in Figure 2.12. Approximately 10,000 muons are stored in the $g - 2$ ring at a time, corresponding to a single fill. The 3.094 GeV muons will decay with a lifetime of approximately 64.4 μs . Once the muons have been injected into the ring, they will begin orbitting clockwise around the ring. By necessity, the inflector must be out of the stored muon beam path, otherwise a large fraction of the muons would be lost upon the return to the injection point as the muons would strike the inflector. Therefore the muon beam must be manipulated to switch the orbit path from the injection orbit onto the central orbit around the center of the storage ring. Once the muon beam is centered, it must also be focused vertically, otherwise all of the muons would be lost due to the vertical motion of the helical path of the muons. To perform the former, a magnetic “kicker” is used to shift the orbits of the muons. To perform the latter, a series of electrostatic quadrupoles focus the beam vertically.

2.5.1 Kicker

The kicker is made up of three separate pulsed magnets located 90° from the exit of the inflector, where the inflector orbit crosses the central orbit. The placement of the kickers is shown in Figure 2.13. It’s important to note that the kicker must be operated within the magnetic field of the ring, and must therefore contain no magnetic elements in the hardware itself which would perturb the uniform magnetic field. For this reason the kicker is made up of thin aluminum plates which carry the current used to create the kicking magnetic field. Due to the bunched nature of the muon beam and the short cyclotron period of 149 ns, ideally the kicker moves all stored muons onto the central orbit and then turns off quickly such that by the time the muons orbit back around to the kicker there is no residual kick to the beam. Any

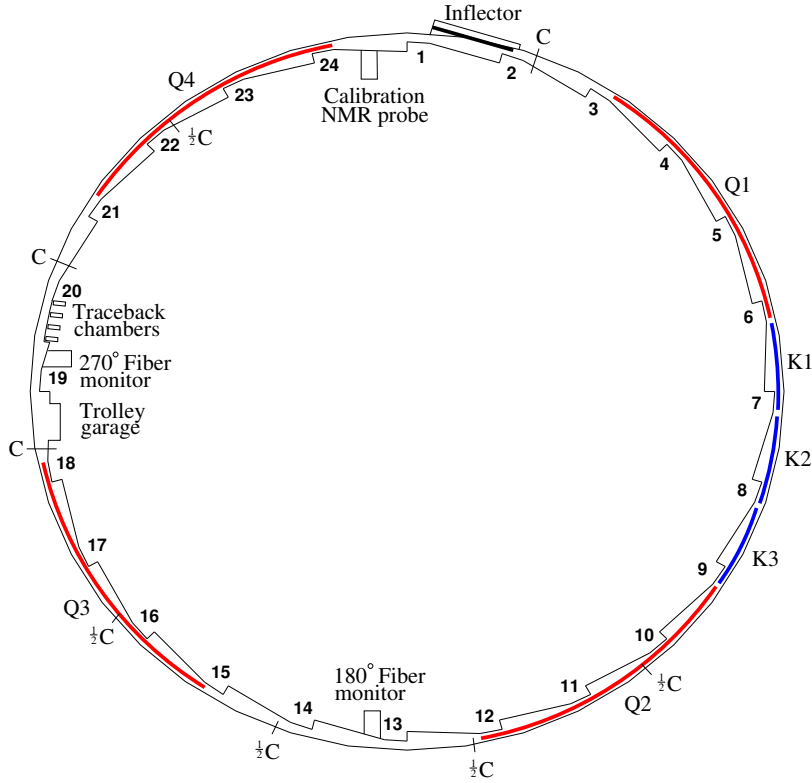


Figure 2.13: A map of the vacuum chambers in E989. K1-K3 show the locations of the kicker magnets, while Q1-Q4 show the locations of the electrostatic quadrupoles. Also shown is the location of the inflector, the two fiber monitors, and one of the tracker stations.

residual eddy currents must die away quickly enough that the magnetic field seen by the stored muons is unperturbed. The kick to the beam is approximately 10 mrad using a vertical pulsed field of around 300 Gauss over three 1.27 m long magnets and with a pulse length of about 120 ns.

2.5.2 Electrostatic quadrupoles

There are four electrostatic quadrupoles (quads) located around the ring as shown in Figure 2.13, which focus the beam vertically and defocus the beam horizontally. (The magnetic field of the ring serves to restore the beam radially in combination with the electric field.) Just as in the case of the kickers, the quads must be operated in the



Figure 2·14: Electrostatic quadrupoles installed into a vacuum chamber [38]. There are four plates mounted to the chamber through insulator standoffs. Also shown are the rails that the magnetic field trolley rides on around the inside of the ring, and between the quad and kicker plates. The distance between opposing quad plates is 10 cm.

vacuum. E989 uses electrostatic focusing elements instead of magnetic ones in order to avoid magnetic field gradients which would limit the precision of the magnetic field measurement. Four quads were chosen in order to maximize the symmetry of the beam motion around the ring. The quads occupy 43% of the ring circumference, leaving space for other elements around the ring. Each quad is made up of two segments, a short segment of 13° and a long segment of 26° . The quads are made out of as little material as possible in order to reduce multiple scattering of decay positrons passing through them. A picture of the quads installed into one of the vacuum chambers is shown in Figure 2·14. A simulation of the equipotential lines of the quads is shown in Figure 2·15. The original design of the quads is detailed in Reference [38].

Lastly, some of the stored muons will be lost during data taking that will affect the measurement of the precession frequency ω_a . In order to reduce the number of lost

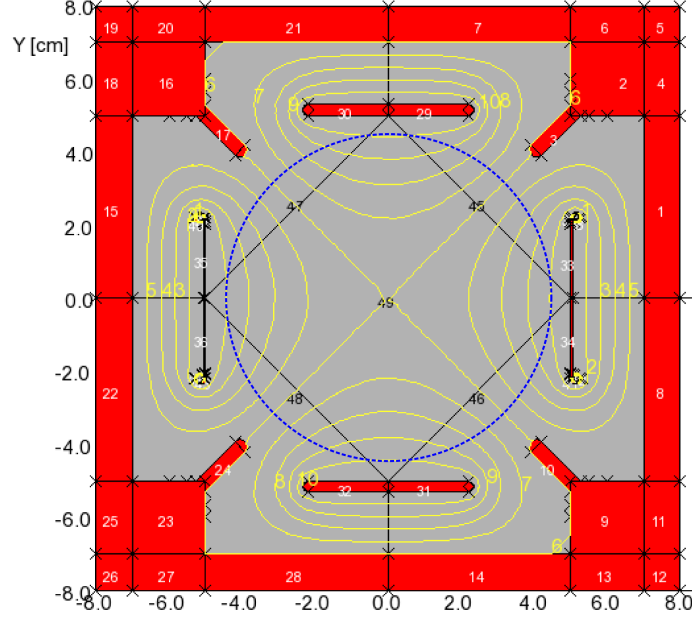


Figure 2.15: An OPERA model of the quads and their equipotential contours. The top and bottom plates sit at positive voltage while the left and right plates are at negative voltage. The muon storage region is shown by the blue circle. Picture from Reference [34].

muons over the course of a fill, a procedure called “scraping” is used to remove those muons sitting at the edge of the storage region that will likely be lost at later times. This scraping procedure involves powering the quad voltages in an asymmetric way such that the beam is pushed to the outside of the storage region, where the edges of the beam will intersect copper collimators. Muons which hit the collimators will lose energy and be lost as they spiral out of the ring. The scraping procedure is performed early in the fill and ends at something $20\text{ }\mu\text{s}$.

2.6 Muon beam dynamics

Muons injected into the storage ring will occupy a region in phase space corresponding to a width of momenta and positions. Individual muons will undergo simple harmonic motion or betatron oscillations within the storage ring, in both the vertical

and horizontal directions. The strength of the electrostatic focusing in relation to the magnetic field strength can be characterized by the field index

$$n = \frac{\kappa R_0}{\beta B_0}, \quad (2.17)$$

where κ is the electric quadrupole gradient, B_0 is the magnetic field strength, R_0 is the central storage ring radius, and β is the relativistic velocity of the muon beam. The horizontal and vertical equations of motion, including the effects of the discrete quadrupoles, are given by

$$x = x_e + A_x(s) \cos(\nu_x \frac{s}{R_0} + \phi_x), \quad (2.18)$$

$$y = A_y(s) \cos(\nu_y \frac{s}{R_0} + \phi_y), \quad (2.19)$$

where x_e is the radial equilibrium orbit of the beam relative to R_0 , $A_x(s)$ and $A_y(s)$ are the amplitudes of the motions containing the effects of the discreteness of the quads, and s is the arc length of the trajectory. Here ν_x and ν_y are the so-called horizontal and vertical “tunes” of the beam motion, which are ratios of the betatron frequencies to the cyclotron frequency. They can be related to the field index n by

$$\begin{aligned} \nu_x &= f_{x_{BO}}/f_c = \sqrt{1-n}, \\ \nu_y &= f_{y_{BO}}/f_c = \sqrt{n}, \end{aligned} \quad (2.20)$$

where f_c is the cyclotron frequency. Technically n is the average field index around the ring, where this approximation is justified due to the four-fold symmetry of the discrete quadrupoles and the fact that the betatron oscillations have periods much greater than the length of the quads. A table of the important frequencies in E989 is shown in Table 2.2. Lastly, the maximum angular acceptance of the ring can be

Muon Beam Frequencies				
Name	Symbol	Expression	Frequency (MHz)	Period
$g - 2$	f_a	$a_\mu Be/2\pi mc$	0.23	4.365 μ s
cyclotron	f_c	$v/\pi R_0$	6.71	149 ns
horizontal betatron	$f_{x_{BO}}$	$\sqrt{1-n}f_c$	6.34	158 ns
vertical betatron	$f_{y_{BO}}$	$\sqrt{n}f_c$	2.21	452 ns
coherent betatron	f_{CBO}	$f_c - f_{x_{BO}}$	0.37	2.703 μ s
vertical waist	f_{VW}	$f_c - 2f_{y_{BO}}$	2.31	433 ns

Table 2.2: Frequencies seen in the $g - 2$ experiment due to beam motion. Parameter values are from a subset of Run 1 corresponding to an n value of 0.108 or a quad voltage of 18.3 kV.

determined from the betatron oscillations and the field index as

$$\begin{aligned}\psi_{x_{max}} &= \frac{x_{max}\sqrt{1-n}}{R_0}, \\ \psi_{y_{max}} &= \frac{y_{max}\sqrt{n}}{R_0},\end{aligned}\tag{2.21}$$

where x_{max} and y_{max} are both equal to the radius of the storage ring aperture at 45 mm.

As the muon beam goes around the ring, the muons will experience local field gradients and inhomogeneities. The tunes are thus chosen to avoid resonances where muons might be lost from having passed through such perturbations too many times. The muons within the ring should then sample the entire azimuth equally and remain stored. The general resonance condition is [39]

$$a\nu_x + b\nu_y = c,\tag{2.22}$$

where a , b , and c are integers. We know from Equation 2.20 that

$$\nu_x^2 + \nu_y^2 = 1,\tag{2.23}$$

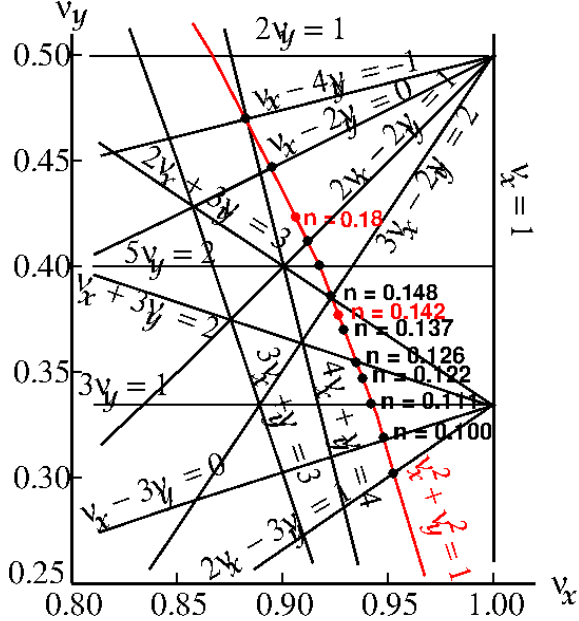


Figure 2.16: The tune plane, with the $v_x^2 + v_y^2 = 1$ constraint in red. The chosen value of n lies on this circle. The original design goals for E989 were the n values as shown by the red points, but due to hardware issues smaller n values of 0.108 and 0.120 were chosen as described in Section 2.8.

which constrains the available n values that can be chosen. Figure 2.16 shows the space relative to the tunes for which a chosen value of n will lie on a resonance.

2.6.1 Coherent betatron oscillation

With each individual muon undergoing betatron oscillations, the muon beam as a whole will oscillate. The beam can be described as having a width and a mean dependent on the initial phase space parameters determined by injection and kicker effects. This overall distribution of the beam will oscillate coherently every betatron wavelength, thus moving around the ring at some frequency. Individual detectors around the ring measure the beam in discrete pieces based on their individual acceptances, where these acceptances depend on the radial and vertical characteristics of the beam. Because the betatron frequencies are smaller than the cyclotron frequency,

there is an aliasing effect such that the betatron motion of the beam is instead observed as an apparent slow-moving oscillation. We call the measurable signal of this coherent radial motion coherent betatron oscillation (CBO). See Figure 2.17 for a pictorial view of this phenomena. The frequency of the CBO is just the beat frequency between the cyclotron frequency and the horizontal betatron frequency

$$f_{CBO} = f_c - f_{x_{BO}}. \quad (2.24)$$

There is also a horizontal CBO effect, but the rate of oscillation is fast enough that the effect tends to average out. What can be seen in the data however is the vertical width of the beam, to which the detectors are sensitive. Though the principles are the same, we call this effect the vertical waist (VW),

$$f_{VW} = f_c - 2f_{y_{BO}}, \quad (2.25)$$

where the term waist is used a description of the vertical width when its at its minimum. Both of these frequencies are included in Table 2.2. For an individual detector the CBO has a specific phase, which goes from 0 to 2π around the ring. When adding all of the detector signals together, the CBO effect tends to cancel out. However, due to acceptance differences between the different detectors, the CBO effect is still observable in the data. When fitting the data to extract ω_a , these effects need to be included as will be discussed later.

2.6.2 Beam debunching

As described above, the muon beam is injected into the ring with a time spread of 120 ns and a range of momenta. At early times the beam will occupy a portion of the ring less than the whole since the cyclotron period is 149 ns. Therefore early in the fill the detectors located at discrete points around the ring will measure counts from the



Figure 2.17: Marked by the black vertical lines are integer steps in the circumference of the ring, corresponding to the cyclotron wavelength λ_c . The blue line shows the motion of the beam due to the betatron oscillations λ_x . Since $\lambda_x < \lambda_c$, there is an aliasing effect in the observed signal, which is identified by the red line. The beam is thus seen as appearing to move back and forth with a slow oscillation, and this is what we call CBO.

beam where there will be a fast oscillation in the signal due to this cyclotron period. As time increases throughout the fill, the momentum distribution of the muons will cause the beam to spread out within the storage ring until the entire azimuth is filled. Since almost all muons are at the same momentum, it turns out that the slower moving muons at smaller radii catch up to the faster moving muons at the outer radii after many turns around the ring. By 30 μs the muon beam has gone around the ring two hundred times. As the beam fills the storage ring, the cyclotron frequency in the data reduces and the beam is seen to debunch. This phenomena is referred to as the “fast rotation.” See Figure 2.18 for how this looks in the data. When dealing with the data and attempting to extract ω_a , the typical procedure is to both bin out the fast rotation in periods of the cyclotron frequency, and to randomize each hit time by $\pm T_c/2$ where T_c is the cyclotron period. In this way the fast rotation is removed entirely and the five parameter function described in Equation 2.13 remains satisfactory, barring other effects.

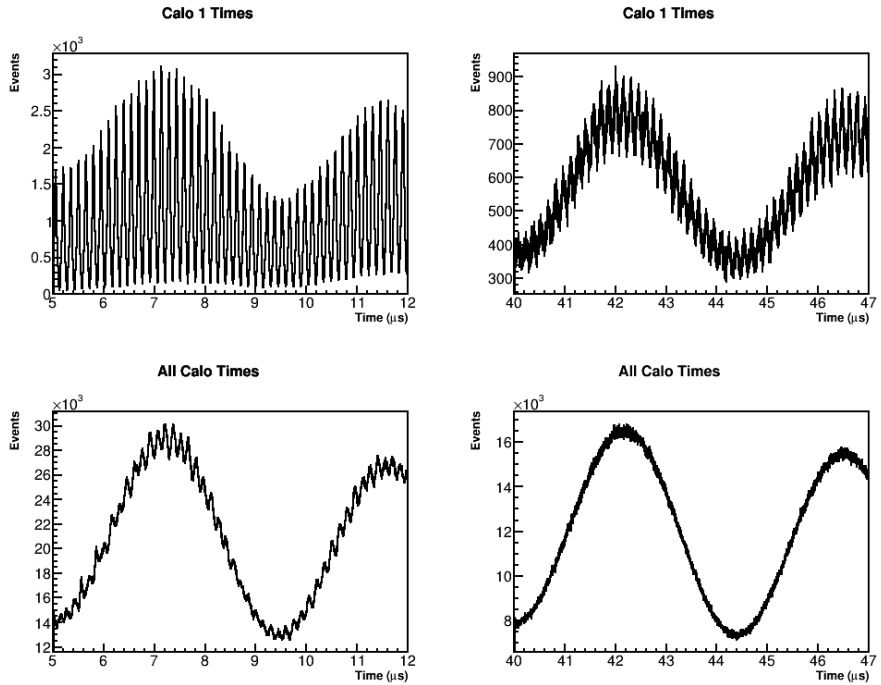


Figure 2.18: The fast rotation signal can be seen in the data as an oscillation with a period of 149 ns, corresponding to the fast oscillations in these plots. In individual calorimeters at early times the fast rotation signal is seen to be very large, as shown on the top left. As time passes and the beam debunches, the amplitude of the fast rotation signal diminishes as shown on the top right. When adding all calorimeters together, the signal reduces as shown in the bottom two plots. In all cases the slow oscillation is the $g - 2$ frequency.

2.7 Corrections to ω_a

Equation 2.3 is an idealized version of the spin difference frequency. Including practical experimental concerns, there are two corrections that must be applied to ω_a .

2.7.1 Electric field correction

In the presence of an electric field, the spin difference frequency is altered to

$$\vec{\omega}_a = -\frac{q}{m} [a\vec{B} - \left(a - \frac{1}{\gamma^2 - 1}\right)(\vec{\beta} \times \vec{E})], \quad (2.26)$$

where now there is an extra term dependent on the electric field strength and the momentum of the particles. This is necessary to include since we use electrostatic quadrupoles for vertical focusing as described above. The second term cancels to first order for a specific momentum or value of γ . This "magic momentum" can be understood as the momentum at which a relativistic particle moving through an electric field has its spin exactly follow its momentum. This magic momentum is 3.094 GeV for muons, hence the momentum value of the injected muons. This value has driven many of the design constraints of the $g - 2$ experiment, including the size of the storage ring, choice of the magnetic field magnitude, and so on.

Not all muons will have the magic momentum however as described in the Section 2.3, and therefore a correction to the measured ω_a frequency needs to be applied. Approximating the storage ring as having an electric field applied over the whole azimuth of the ring, the spin difference frequency for muons with momentum $p \neq p_m$ (where p_m is the magic momentum) becomes

$$\omega'_a = \omega_a \left[1 - \beta \frac{E_r}{cB_y} \left(1 - \frac{1}{a\beta^2\gamma^2} \right) \right]. \quad (2.27)$$

Here the motion of the beam is assumed purely azimuthal. This additional term is the electric field correction that then serves to lower the measured ω_a frequency. Using

the relation $p = \beta\gamma m = (p_m + \Delta p)$, after a little bit of simplification the electric field correction can be written as

$$C_E = \frac{\Delta\omega_a}{\omega_a} = -2\frac{\beta E_r}{cB_y} \frac{\Delta p}{p_m}. \quad (2.28)$$

The last fraction can be related to the field index described in Equation 2.17 by

$$\frac{\Delta p}{p_m} = (1 - n) \frac{\Delta R}{R_0} = (1 - n) \frac{x_e}{R_0}, \quad (2.29)$$

since we know that the magic momentum muons live at the center of the storage ring radius R_0 . In this equation $x_e = \Delta R$ is the equilibrium radius of the beam relative to the central storage radius. Noting that the electric field strength is

$$E = \kappa x = \frac{n\beta c B_y}{R_0} x, \quad (2.30)$$

and assuming that it is perfectly radial, the electric field correction can be reduced to

$$C_E = -2n(1 - n)\beta^2 \frac{xx_e}{R_0^2}. \quad (2.31)$$

Taking the time average of the beam motion, where x is simply equal to x_e , then the correction becomes

$$C_E = -2n(1 - n)\beta^2 \frac{\langle x_e^2 \rangle}{R_0^2}. \quad (2.32)$$

This electric field correction can be determined through analysis which relates the beam momentum to the equilibrium radius. (Should I expand on that somehow here?) The assumptions made here are sufficient for the $g - 2$ measurement [something].

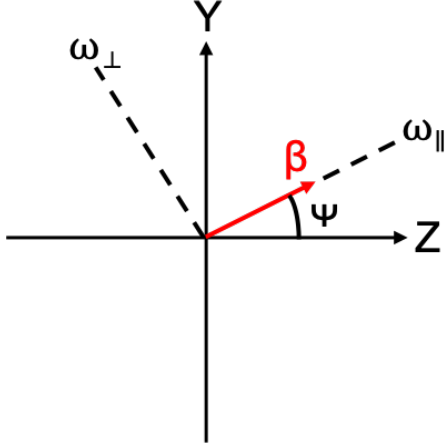


Figure 2.19: Beam motion β relative to the vertical and azimuthal axes Y and Z respectively. ψ is the pitch angle of the beam, and the dashed lines represent the parallel and perpendicular motions of the beam.

2.7.2 Pitch correction

Particles injected into the $g - 2$ storage ring will have some motion component that is vertical, or parallel to the magnetic field vector (hence the need for vertically focusing electrostatic quadrupoles). This will reduce the magnetic field seen by the muons in their rest frame slightly. Including this motion into the spin difference frequency (along with the electric field correction described previously), ω_a becomes

$$\vec{\omega}_a = -\frac{q}{m} [a\vec{B} - a\left(\frac{\gamma}{\gamma+1}\right)(\vec{\beta} \cdot \vec{B})\vec{B} - \left(a - \frac{1}{\gamma^2-1}\right)(\vec{\beta} \times \vec{E})], \quad (2.33)$$

where now there is an extra term in the middle dependent on the vertical betatron motion of the beam. Similar to the electric field case, this term can be neglected to first order as the muon momentum is nearly all perpendicular to the field, but a correction again needs to be applied to ω_a to account for this effect.

Since the muons in the storage ring will be oscillating vertically as they are focused by the quads, their momentum vectors will be pitching up and down relative to the

azimuthal motion. This pitch angle will oscillate as

$$\psi = \psi_0 \cos(\omega_y t), \quad (2.34)$$

where ψ_0 is the amplitude of the oscillation and ω_y is the vertical betatron frequency. Shown in Figure 2.19 is an exaggerated example of the beam motion relative to the vertical and azimuthal axes. Assuming that the field is purely vertical, $\vec{B} = B_y \hat{y}$ and that the beam motion is in the vertical-azimuthal plane,

$$\vec{\beta} = \beta_y \hat{y} + \beta_z \hat{z} = \beta \cos(\psi) \hat{y} + \beta \sin(\psi) \hat{z}, \quad (2.35)$$

then ω_a becomes

$$\vec{\omega}_a = -\frac{q}{m} [a B_y \hat{y} - a \left(\frac{\gamma}{\gamma + 1} \right) \beta_y B_y (\beta \cos(\psi) \hat{y} + \beta \sin(\psi) \hat{z})], \quad (2.36)$$

where in this case the electric field part has been ignored. Using the small angle approximation such that $\cos(\psi) \approx 1$ and $\sin(\psi) \approx \psi$, $\vec{\omega}_a$ can be separated into its vertical and azimuthal components

$$\omega_{ay} = \omega_a \left[1 - \left(\frac{\gamma - 1}{\gamma} \right) \psi^2 \right], \quad (2.37)$$

$$\omega_{az} = -\omega_a \left(\frac{\gamma - 1}{\gamma} \right) \psi. \quad (2.38)$$

Looking at Figure 2.19 again, it can be seen that the spin difference frequency can be resolved into its parallel and perpendicular components ω_{\parallel} and ω_{\perp} respectively. As the pitch angle of the beam motion oscillates about the azimuthal axes at a frequency much greater than the $g - 2$ frequency, it can be seen that the parallel component averages to 0 over time. (Haven't given a number for the vertical betatron frequency yet.) We then only care about the perpendicular oscillation of the beam, which can

be determined with a simple rotation matrix such that

$$\omega_a \approx \omega_{\perp} = \omega_{ay} \cos(\psi) - \omega_{az} \sin(\psi) \approx \omega_a \left[1 - \frac{\psi^2}{2} \right], \quad (2.39)$$

where in the last approximation the small angle approximation was used once again, but this time with $\cos(\psi) \approx 1 - \psi^2/2$. The pitch correction then is the additional term which serves to lower the measured spin difference frequency. Taking the time average,

$$C_P = \frac{\Delta\omega_a}{\omega_a} = -\frac{\langle \psi^2 \rangle}{2} = -\frac{\langle \psi_0^2 \rangle}{4}, \quad (2.40)$$

where Equation 2.34 was used in the last equality. The pitch angle of the beam cannot be measured directly, however we know from Equation 2.21 that the angle of the beam can be related to the vertical distribution of the beam, such that

$$C_P = -\frac{n}{4} \frac{\langle y^2 \rangle}{R_0^2}. \quad (2.41)$$

Once again n is the field index, R_0 is the radius of the ring at the center of the storage region, and $\langle y^2 \rangle$ is the vertical width of the beam. The first two are known and the last can be measured experimentally. (For this last equation make sure that what I write here gels with what I'll put in other sections, which haven't been done yet.) While this derivation was an approximation assuming continuous quads around the ring, it suffices for the level of precision necessary for the $g - 2$ experiment [something].

2.8 Run 1 in E989

Run 1 for E989 was conducted in the first half of 2018. Production data was gathered from March 22nd through June 29th. Because of accelerator, experimental, and practical concerns production data taking was interrupted at various dates. Due to hardware issues both kicker and quad settings were lowered from their original design

values. Stable voltage set points were identified and used in separate periods of the data taking, depending on the stabilities of the systems. The distinct datasets and their associated parameters are shown in Table 2.3. For Run 1, n values of 0.108 and 0.120 were chosen corresponding to quad voltages of 18.3 and 20.4 kV respectively [40]. The associated betatron wavelengths are 1.06 and 3.04 times the circumference of the storage ring respectively.

From kicker section: In Run 1 the kickers were not able to be run at the design voltage necessary to put the beam exactly on the central orbit. Instead the beam is kicked to a stable orbit a couple of mm off center depending on the actual value of the kick used, as shown in Figure 4.7. (**Clarify what the exact numbers are here, or point to the section where I describe the values used in Run 1.**)

From quad section: During Run 1 it was discovered that some of the quad resistors were damaged, leading to longer RC time constants such that the quad voltages had not returned to storage nominal during the designated analysis portion of the data. (**Show a picture here of those time constants?**) Note that despite this scraping procedure, some stored muons are still lost anyways. The effects on the measurement of ω_a due to this are explored in Section ??.

-number of muons per fill number somewhere...

[41]

Run 1 Datasets						
Name	Number $e^+ > E_{\text{Th}}$	n	Value	Quad Voltage (kV)	Kicker Voltage Range (kV)	f_{CBO} (MHz)
60H	9.3×10^8		0.108	18.3	128 to 132	0.37
HighKick		0.120		20.4	136 to 138	
9d	2.2×10^9		0.120	20.4	128 to 132	
LowKick		0.120		20.4	123 to 127	
SuperLowKick		0.108		18.3	117 to 119	
Endgame		0.108		18.3	122 to 127	

Table 2.3: Update the number of positrons column once all of the datasets have been opened and energy thresholds chosen. Potentially also add further columns of interest or split into multiple tables.

Chapter 3

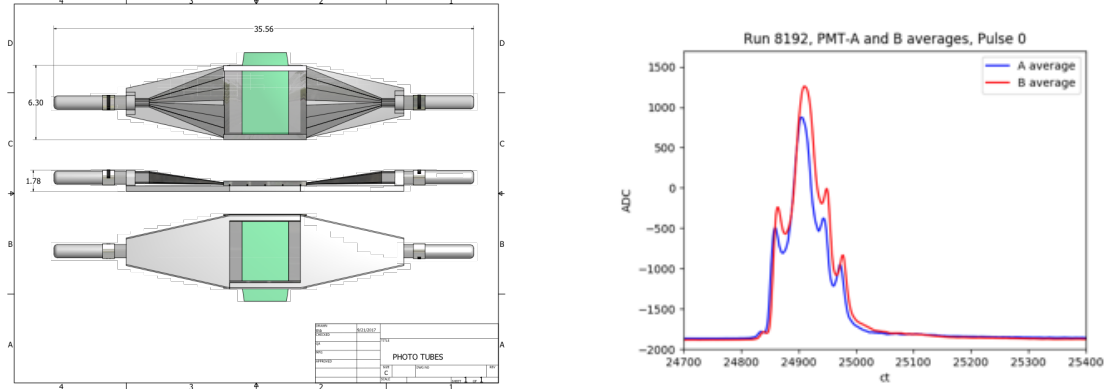
Detector Systems

There is a variety of different detector systems used in E989. The primary detectors are the calorimeters which measure the ω_a signal. In support of that measurement there are several auxiliary systems used for monitoring injection and beam dynamics. These include the T0, IBMS, and fiber harps. There is also a straw tracking detector which measures decay positron trajectories which can be related to muon beam dynamics and calorimeter measurements. Each of these systems will be described in the following sections.

3.1 Auxiliary detectors

3.1.1 T0

During data taking, a reference time must be chosen so as to align all different detector systems in time. When taking data from fill to fill, decay positron spectra must be aligned in phase. Without this functionality, analyzing the data from different systems and comparing them would be impossible. To do this a “T0” counter is placed just on the outside of the ring before the inflector. It is made up of a scintillating paddle connected to two photo-multiplier tubes (PMTs) [42, 43]. See Figure 3·1a. One PMT, PMT A, has a 1% neutral density filter resulting in low photo-electron statistics, and acts primarily as a timing measurement. The other, PMT B, has a 10% neutral density filter resulting in higher statistics, and acts as a shape counter and proxy for fill intensity. (In general the signals are very similar.) Together they provide a



(a) The T0 counter is made up of a scintillator in the middle shown in green, which connects with light guides to PMTs on the left and right.

(b) Time profiles for the two PMTs in the T0 counter for one of the eight bunches we receive at a time as described in Section 2.3. Each profile is an average of 100 such profiles. The x axis is in clock ticks, each of which is 1.25 ns.

Figure 3.1: A model of the T0 detector (left) and the signal it measures per fill (right).

measure of the injected beam profile in time, allowing to align the detectors each fill, and the data from fill to fill. Some measured T0 pulses are shown in Figure 3.1b. The shape of the incoming pulses has a somewhat trident-like shape, with a very large spike in the middle of the time width, and two spikes on the outside edges. This shape owes itself to the accelerator complex, and varies from bunch to bunch.

3.1.2 Inflector Beam Monitoring System

While the T0 provides timing and intensity measurements, the inflector beam monitoring system (IBMS) provides measurements of the beam position properties as it passes through the inflector. This is useful because the injection aperture is so tight, and incoming beam parameters are tightly constrained. The IBMS system serves to provide a direct diagnostic handle on the phase space matching between the last accelerator components and the $g - 2$ storage ring, helping to optimize the number of stored muons per fill [44]. The IBMS is made up of two scintillating fiber detectors,

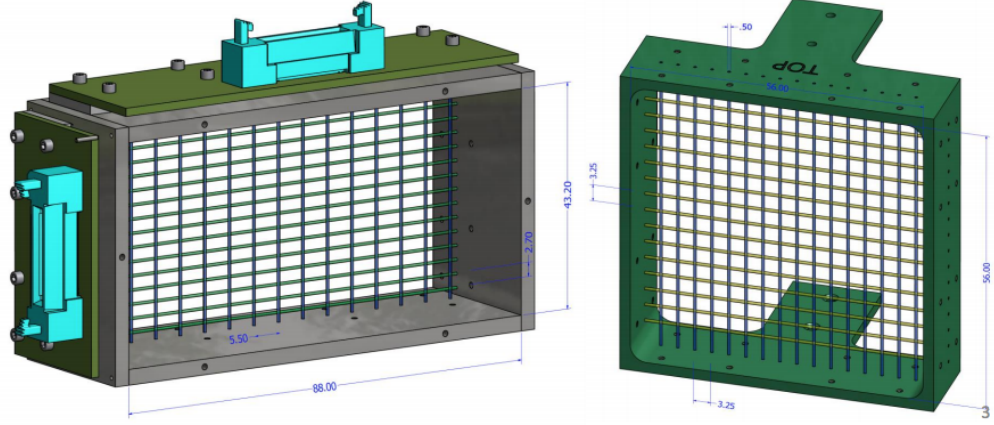


Figure 3.2: Models of the IBMS 1 and 2 detectors. Scintillating fibers form an array which detect particles as they pass through them.

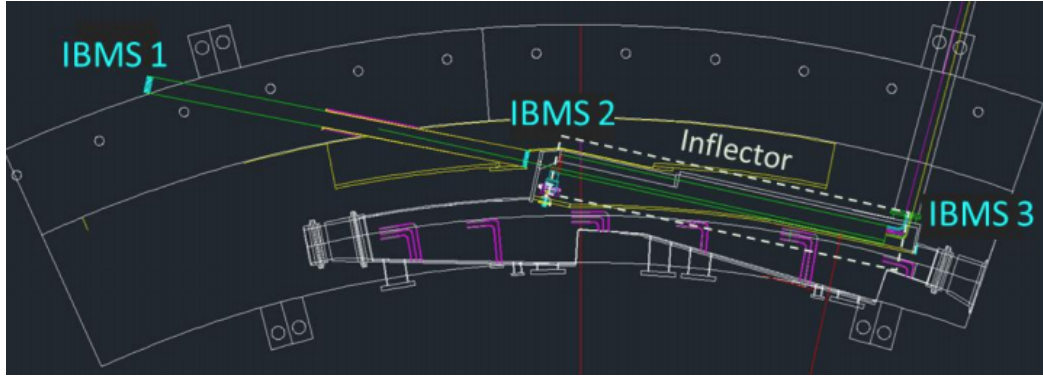


Figure 3.3: The positions of IBMS 1, 2, and the planned 3rd device are shown with respect to the vacuum chamber and inflector.

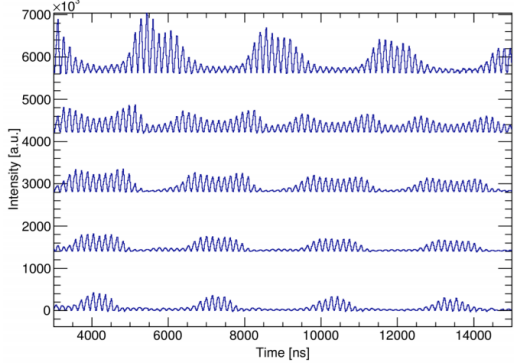
as shown in Figure 3.2. These devices are placed at the outside of the magnet yoke before injection into the back hole of the magnet, and at the entrance to the inflector [45]. A third device is planned to be at or near the downstream end of the inflector. See Figure 3.3.

3.1.3 Fiber harps

The last auxiliary detector is the so called “fiber harp” system. It is made up of four scintillating fiber detectors located within the ring that serve to measure the beam intensity as a function of time and position [46]. Two of the detectors measure the ra-



(a) Picture of one of the fiber harps. A row of seven scintillating fibers measures the beam intensity as a function of time at vertical or horizontal positions depending on which fiber harp is inserted.



(b) Shown are fiber harp beam intensity measurements for the horizontal fiber harp. Each spectra is from a single fiber, with the spectra at the top being at the greatest radial positions. The fast oscillations of the cyclotron frequency can be seen along with the slower oscillations of the CBO.

Figure 3·4: Fiber harp detector (left) and a sample of fiber harp measurements (right). **Figure out how to move left picture up, or maybe rethink this figure entirely.**

dial components of the beam, and two measure the horizontal components. The fiber harps are located at positions 180° and 270° clockwise from the inflector. One of these devices is shown in Figure 3·4a. The fiber can measure beam properties throughout the fill, providing a diagnostic tool which is sensitive to the scraping procedure and the CBO properties of the beam. An example of fiber harp measurements is shown in Figure 3·4b. However because the fiber harps are a destructive measurement of the beam due to multiple scattering in the fibers, the system was designed to be retractable. They are inserted during special diagnostic or systematic runs, and are pulled out of the beam path during production data taking.

3.2 Calorimeters

Electromagnetic calorimeters are the primary detector in the E989 experiment, responsible for the ω_a measurement. They measure hit times and energies of decay positrons as they curl inward from the storage region.

3.2.1 Requirements and systematic effects

In order to determine ω_a to the precision goal, there are specific requirements on the performance of the calorimeters. First, they must have a relative energy resolution of better than 5% at 2 GeV, in order for proper event selection above threshold [34]. The energy resolution requirement is modest but not strict because the important observable is the number of detected positrons above some energy threshold, where the optimal energy threshold can be determined empirically.

Second, they must have a timing resolution of better than 100 ps for positrons with energy greater than 100 MeV [34]. The calorimeters must be able to resolve multiple incoming hits through temporal or spatial separation at 100% efficiency for time separations of greater than 5 ns, or 66% of hits for time separations less than 5 ns, in order to reduce the pileup systematic effect. Pileup is the term used for when multiple particles impact the detector within the deadtime of the detector such that they are registered as a single hit. Unresolved pileup means that the number of detected positrons above threshold is mis-measured. Since pileup is a time-dependent effect, where pileup decays at some lifetime approximately equal to half the muon lifetime, this leads to a mis-measurement of ω_a . The requirements stated here assist in reducing the pileup systematic error below a target goal of 40 ppb.

Third, the energy response of calorimeters for measured hits must be stable to $< 0.1\%$ over a fill (700 μ s) [34]. The long term energy response stability over a time period of order seconds must be $< 1\%$. The energy response of a detector as a

function of time is typically referred to as the gain of the detector, where technically the gain refers to the amount of current output per detected hit. The gain depends on the temperature stability and hit rate. After a hit, the measured energy fraction of a following hit drops sharply and then rises exponentially back to one. This is referred to as the short-term double pulse (STDP) effect. At injection many particles are injected into the ring and there is a large amount of secondary particles incident in the calorimeters. The accumulation of all the individual STDP effects ends up causing a large gain drop at the beginning of each fill. This is typically referred to as the in-fill gain (IFG) effect. Hits with mis-measured energies due to these effects can thus be excluded from the fitted histogram if their energies drop below threshold, leading to another systematic effect and subsequent error in the ω_a measurement. (Temperature changes vary over time scales greater than a fill, so don't contribute to the systematic error.) The requirements stated here, along with the use of a laser calibration system (Section 3.2.3), assist in reducing the gain systematic error below a target goal of 20 ppb.

3.2.2 Harware

There are 24 calorimeters located symmetrically around the inside of the ring placed flush to the vacuum chamber wall, as shown in Figure 3.5a. (Indeed the shape of the vacuum chambers were designed so as to reduce multiple scattering of the decay positrons before entering the calorimeters.) Each calorimeter sits on a board extending out from a cart which contains the electronics that power the calorimeters and read out the data. The carts help to relocate magnetic materials away from the field region to avoid perturbing the magnetic field, and provide easy access to the electronics while removing them from the positron decay path region.

Each calorimeter consists of 54 channels of PbF_2 crystals arrayed in a 6 high by 9 wide array, for a total of 1296 channels. Each crystal is $2.5 \times 2.5 \times 14 \text{ cm}^3$ and



(a) In black are the calorimeter carts, which house the electronics for the calorimeters. They hold up a board upon which the calorimeter rests. The calorimeter as shown is pushed flush to the vacuum chamber on the left.

(b) Shown is the backside of a calorimeter. The clear blocks are the PbF₂ crystals, each of which has a SiPM mounted onto the back of them.

Figure 3.5: Calorimeter systems relative to the vacuum chamber (left) and an individual calorimeter (right). **probably update these pictures at some point**

is wrapped in black Tedlar® foil. The PbF₂ material has an index of refraction of 1.8, and emits Cerenkov light as incident positrons with energy greater than 100 keV pass through the crystals [47]. Cerenkov light is naturally fast which improves the timing resolution of the incoming hits. The high density of the PbF₂ gives it a short radiation length, such that the energy deposition from the incident positrons is nearly 100% over the length of the crystal. The black foil is used to reduce light transmission between crystals and improve position reconstruction, as well as reduce pulse width [48]. The energy deposition from the incident positrons is typically restricted to only one or two crystals. The segmentation of the calorimeter combined with the black wrapping helps the spatial and temporal resolution of the detected pulses. See Figure 3.5b for a picture of the calorimeter crystals.

Each crystal is paired with a large area silicon photo-multiplier (SiPM) sensor which reads out the emitted Cerenkov light. SiPMs are compact, operable in high

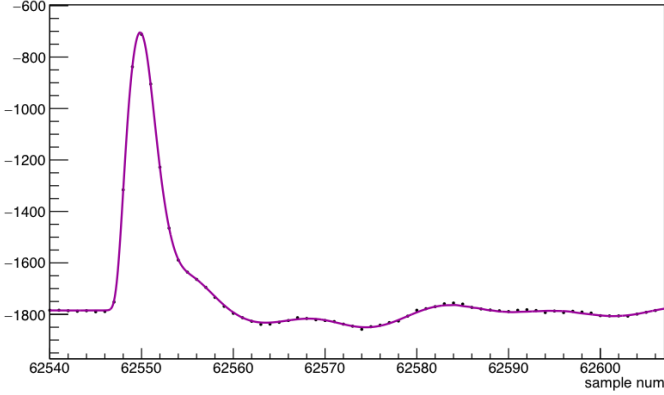


Figure 3.6: Output pulse from a SiPM in black dots, overlayed with a fit template.

magnetic field regions, have very linear responses for operation at MHz rates, are suited to measuring Cerenkov light due to their high photo-detection efficiency in the wavelengths of interest, and have a high degree of gain stability [48]. The SiPMs used are designed by Hamamatsu and detailed in Reference [48]. They sit on printed circuitry boards (PCBs) devoid of magnetic materials, which are designed to preserve the fast SiPM pulse shape. The combined properties of the chosen SiPMs, their electronic boards, and the PbF_2 crystals results in an energy resolution of $(4.6 \pm 0.3)\%/\sqrt{E/\text{GeV}}$, a timing resolution of 20 ps, and a pulse width of 5 ns, satisfying the stated requirements earlier [47, 48]. Details of the pulse fitting algorithms are shared in Section 5.2. The SiPMs can be seen in Figure 3.5b. Finally, 12-bit waveform digitizers (WFD) sample each SiPM channel at a rate of 800 mega-samples per second with a 1 Gb memory buffer and the data are transferred to a bank of GPU processors for on-line data processing [49]. The timing resolution of these WFDs is < 50 ps for most pulse amplitudes. A typical pulse from an incident positron is shown in Figure 3.6.

3.2.3 Laser calibration system

In order to satisfy the gain requirements of the calorimeter detectors, a laser calibration system is used. This system monitors the SiPM responses over short and long time scales to $< 0.04\%$ [50]. The system consists of six different lasers and a suite of optical devices. The light from the six lasers is piped to a board mounted on the front face of each calorimeter through optical fibers. This board contains right-angle prisms which it uses to deflect the laser pulses directly into each calorimeter crystal, for all 1296 channels. The lasers can be pulsed at various intensities, both in-fill to monitor the STDP or IFG effects, and out-of-fill to monitor for long term drifts due to changing temperatures or detector degradation. The SiPM measured response is compared to local known source monitors in order to calibrate the SiPM energy response. Corrections to the gain of the calorimeters can thus be determined and applied to the hit energies. Simultaneously the laser system allows for measuring the timing resolution of the SiPMs, and in general performing diagnostic tests with the calorimeter. Lastly, the laser system is used to time align the different calorimeter channels by outputting a sync pulse to each channel at the beginning of every muon fill.

3.3 Straw trackers

As described in Section 2.6, the muon beam moves as a whole within the storage ring. As explained in Section 2.2, the muon beam distribution ties into the measurement of the magnetic field. The primary detector system used to measure this behavior and determine the muon beam distribution is the “straw tracker” system. The straw trackers characterize the beam in a non-destructive fashion by measuring decay positron trajectories and extrapolating them back into the storage ring. They serve to provide the direct measurement of the pitch correction as described in Section 2.7.2,

determine the momentum distribution of the beam, and characterize parameters of the CBO which tie into the calorimeter ω_a analysis. Decay positron trajectories can also be extrapolated forwards into the calorimeter, in order to cross-check calorimeter measurements to help resolve pileup. Finally, the trackers also serve as a measuring device to search for a possible muon electric dipole moment. The existence of such a thing would tilt the precession plane of the muons and subsequent decay positron trajectories which the trackers are sensitive to. Details of the beginnings of such a search are given in Reference [51]. The details of the track reconstruction and analysis will be given in Chapter 4. Here will be given a description of the detectors themselves and how they work.

In general, straw tracking detectors work by measuring hits in gas filled straws [52]. Each straw is made up of a cylindrical piece of thin conducting material, typically Mylar, and contains a wire at the center of the straw held at high voltage, $\mathcal{O}(1000\text{ V})$. The minimal amount of material in straw trackers serves to reduce multiple scattering of incident particles, and was the reason a straw tracker system was chosen over other tracker types. Fast moving particles ionize the gas as they pass through it, and the resulting ions are drawn to the wire and straw surface (positive and negative charges respectively). As the ions move to the wire, they enter a high electric field region which causes them to speed up, hit other gas molecules, and create more ions. This produces an avalanche gain effect which amplifies the original signal. Once the ions reach the wire and straw surface, a signal is read out telling what the drift time of the ions was, which can be related to the radius or distance of closest approach (DCA) the particle passed relative to the wire. The straws therefore measure drift circles in a plane perpendicular to their physical orientation. By combining several such signals in time and space, we are able to reconstruct tracks of incident particles. See Figure 3.7.

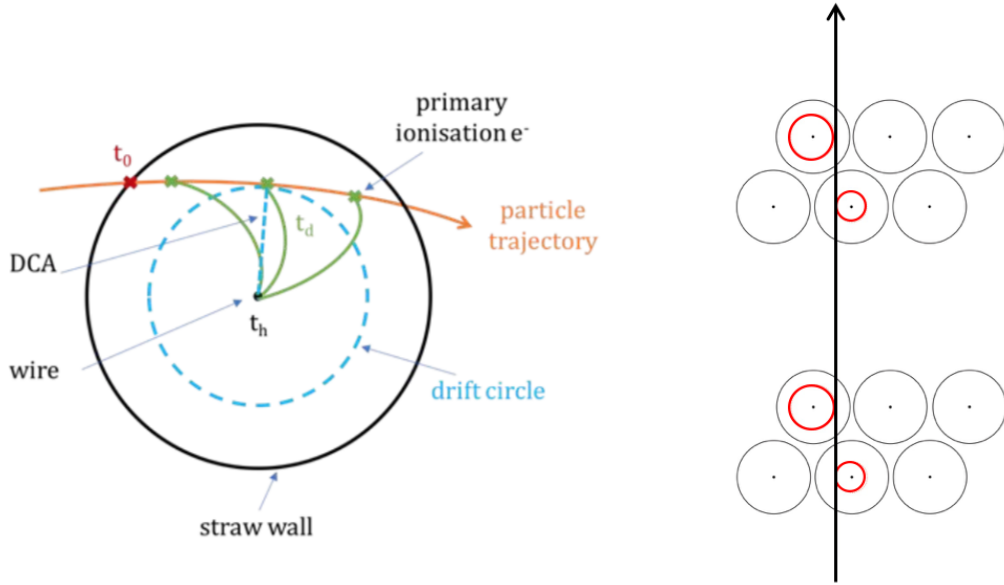


Figure 3.7: Diagrams showing the determination of a drift time t_d and hit time t_h from an incident ionizing particle (left) and the combination of several such hits to produce a track (right). Diagram on left courtesy of Saskia Charity.

Our straws are 5 mm in diameter and contain a 50:50 mixture of argon-ethane gas [53]. The argon component serves as the gas to be ionized. The fast moving ions near the wire in addition to producing more ions, will incite excited states of the gas, which emit photons when de-excited. These photons can restart the whole ionization and avalanche process over again as they can escape the avalanche region, leading to a break-down of the system. The ethane therefore serves to absorb the photons with its large number of molecular degrees of freedom and photo-absorption characteristics [53]. The wire has a radius of 25 μm and is made up of gold-plated tungsten. The Mylar walls have a width of 15 μm and are wound in a double spiral shape in order to improve the electrostatic shielding of the wire and reduce the gas leak rate of the straws [53]. The position resolution of hits within the straws is approximately 150 μm [something].

A single tracker module is shown in Figure 3.8. Each tracker module consists of

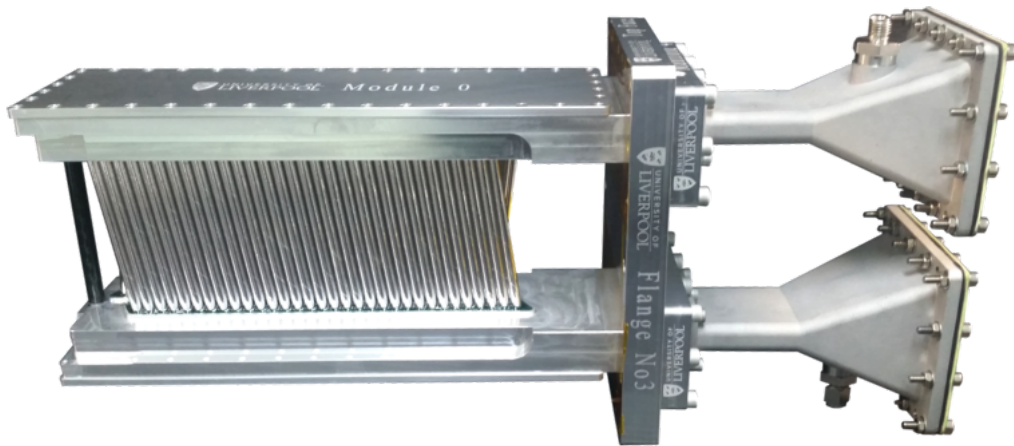


Figure 3·8: A straw tracker module. The first layer of silver Mylar straws with a stereo angle of 7.5° can be seen, with the other three straw layers hiding behind it. In black on the left is the carbon fiber post which holds the end of the module in a fixed position. Electronics live in the top and bottom manifolds above and below the straws, and cables connect from those electronics through small apertures to external electronics which plug in on the right.

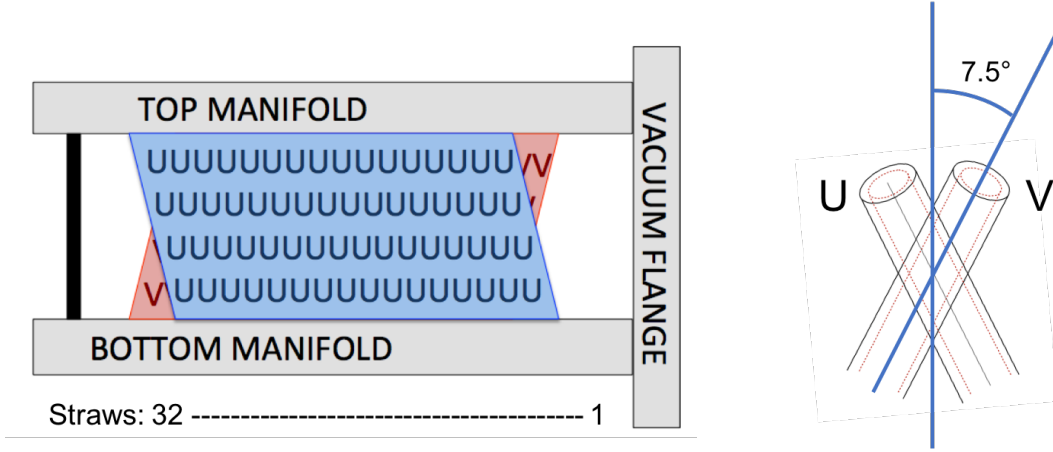


Figure 3.9: Orientation of U and V straws in the tracker module.

4 layers of 32 straws each with stereo angles of $\pm 7.5^\circ$, for a total of 128 straws per module. The first two straw layers are designated as “U” layers, and are oriented with the tops of the straws at a greater radial position than the bottoms of the straws. The second two layers are designated as “V” layers, and are oriented with the bottoms of the straws at a greater radial position than the tops. Both U or V layers are collectively referred to as the U and V views of the module respectively. See Figure 3.9. The two layers in each view are shifted half a straw diameter horizontally from one another in order to help resolve which side of the wire any incident particles passed, Section 4.2.3. The two types of layers are non-parallel to each other in order to resolve incident tracks in 2D space. The small stereo angle both improves the straw measurement area as electronics can be kept out of the positron decay path region, and improves the radial momentum resolution of the fitted tracks, since both views measure mostly in the horizontal plane. The active straw measurement area is approximately 10 cm high by 20 cm wide. A carbon fiber post sits at the outside end of the module to provide structural rigidity to the module, and keep the straw wires under tension.

There are two tracker stations, each consisting of eight tracker modules. The two

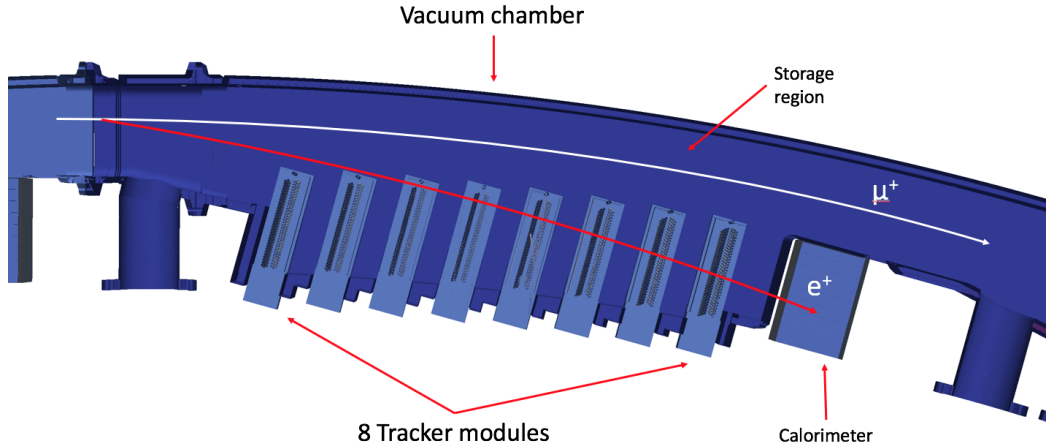


Figure 3·10: Birds eye view of a model of a vacuum chamber containing a tracker station, and the associated calorimeter. Each tracking station consists of eight tracker modules.

stations live at positions in front of calorimeters 13 and 19, or at approximately 180° and 270° clockwise from the inflector. There is also a third station just after the inflector, which currently sits empty of any tracker modules. The straw tracker modules sit inside the vacuum chamber in specially modified vacuum chamber sections in a staircase-like pattern that follows the curvature of the ring. See Figure 3·10. The number of modules and their orientation in each station was chosen to provide a long measurement arm for precise momentum measurement of the incident tracks. The modules sit inside the vacuum in order to eliminate multiple scattering in air and produce better reconstructed tracks. Due to their proximity to the storage region, the tracker modules also live in a region of high field non-uniformity. Though the acceptances between the trackers and calorimeters are not identical, their close proximity facilitates comparison between the two measurement devices. Finally, even though the tracker stations live at only two places in the ring, they measure the average beam distribution due to the CBO motion of the beam and the long extrapolation distance of the measured trajectories.

3.3.1 Tracker readout electronics

The readout electronics for the system are split into two groups, the front-end and back-end. The front-end electronics were built and tested at the Boston University Electronic Design Facility. They start with Amplifier Shaper Discriminator with charge (Q) (ASDQ) chips on boards that plug down directly onto the straws and provide the main signal. Each ASDQ plugs onto sixteen straws. These ASDQ boards are application specific integrated circuits (ASICs) which read out the signal from one end of the straws and shape and discriminate that signal, as well as providing some baseline restoration and tail cancellation. The ASDQs and their associated components live in thin aluminum manifolds above and below the straws. The physical footprint of these boards and components was minimized in order to increase the straw measurement area. The signals from the ASDQs are passed through Flexi Cables to Time to Digital Converter (TDC) boards which time stamp the signals with 625 ps precision [53]. The Flexi Cables are flexible and thin such that the cables can be passed through the thin aperture shown on the right of Figure 3.8. High voltage is provided to the sense wires with high voltage boards, which pass the voltage through the ASDQs. A feedthrough board provides the interface between the TDCs and Flexi Cables, as well as the high voltage signal. They serve a dual purpose of providing the gas seal. Finally, there are logic boards that serve as the interface between the TDCs and the back-end electronics. They manage the clock and controls for the TDCs and store data onto FPGAs, which is piped out through a high throughput optical fiber connection. The logic boards, high voltage boards, and TDCs are all housed within an aluminum box which provides RF shielding. In each module there are eight ASDQs, four TDCs, two feedthrough boards, two high voltage boards, and two logic boards. An overview diagram of the front-end readout chain is shown in Figure 3.11. The back-end electronics consist of FC7s, one per tracker station, and a single AMC13

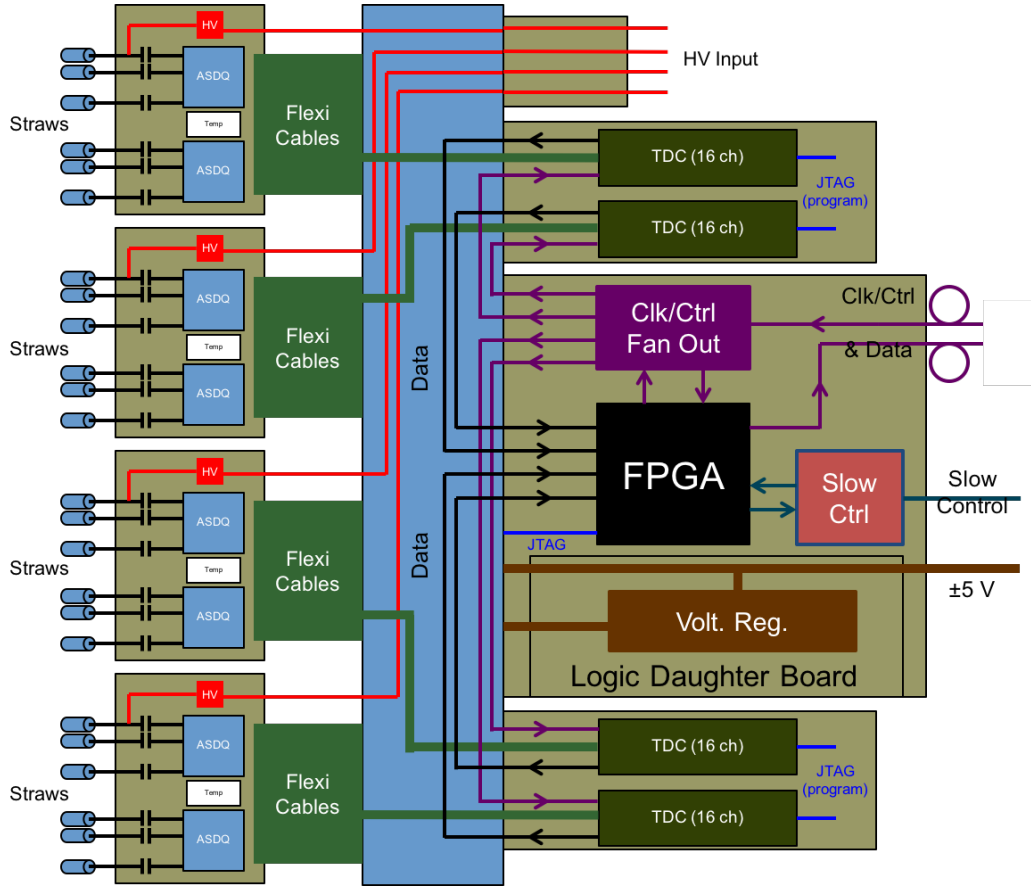


Figure 3.11: Front-end tracker electronics readout chain. Created by James Mott.

for all tracker stations. These modules provide clock and DAQ services to the whole tracker system, and ultimately pipe out the data to where it can be saved on disk.

Chapter 4

Track Reconstruction and Analysis

As described in section 3.3, the straw trackers are used to provide information about the muon beam, important for the calorimeter ω_a analysis, calculating the ω_a pitch correction, and determining the spatially weighted magnetic field seen by the muons. The track reconstruction is performed in three stages: First, individual hits in the tracker are grouped into individual tracks in the finding stage. Second, a best trajectory is fit to grouped hits in the fitting stage. Third, the best fit trajectory is extrapolated back to the storage region or forwards to the calorimeter in the extrapolation stage. A fourth refinement stage is planned but not yet implemented, which would add or remove hits in the finding stage based on the results of the fitting and extrapolation stages.

As a brief aside, every stage of the track reconstruction is performed in the event-processing framework known as *art* [54]. The *art* framework is a collection of modularized stages in a C++ framework useful for reading, reconstructing, filtering, analyzing, and writing data, among other things. All Fermilab experiments now use *art*, and E989 is no exception.

4.1 Track Finding

The track finding stage consists of pattern recognition routines in order to group individual hits into separate sets corresponding to individual incident tracks. The general implementation of these pattern recognition routines is relatively straightforward [55,

[56]. Hits across all modules are grouped in time windows called time islands, with a max width of 100 ns. Within those time islands hits are then grouped into clusters. Clusters consist of one or two hits for each U or V view per module. As a reminder the U and V views of a module consist of the two U or V layers in that module, Section 3.3. Hits are only clustered if they lie in close proximity in time and space to one another. The spatial constraint is defined as the difference in hit straw numbers, from 0 to 31 for the 32 straws per layer, which by default is limited to less than or equal to 4. Neighboring hit clusters in the same module are then grouped to form seeds, one per module. Finally, seeds in successive modules are grouped starting from one end of the tracker to form what are called track candidates. The seeds are formed and grouped into track candidates again only if they lie close in time and space to one another. The entire track candidate formation process occurs for all hits in a time island to find as many real tracks as possible. See Figure 4·1.

After a track candidate has been formed a number of checks are made before passing it on to the fitting stage. If hits, clusters, or seeds are found to be shared among multiple track candidates, the candidates are dropped. Likewise, a track candidate is dropped if it is made from seeds consisting of only one type of view, or if the track candidate has less than six hits. There are also various small geometry and timing algorithms to improve the track candidates, such as removing hits from secondaries [57]. The t_0 time for the track candidate is calculated as the mean time of all hits, with some fixed offset at the end. This t_0 is helpfully constrained by geometry effects, where for a straight track passing through two layers in the same view, the sum of the drift times adds up to a constant (cite or show this?). The track candidate is supplied with an original momentum and position guess at the start of the track by fitting a circle to the hit straw wires in the horizontal plane. The final track candidates are passed on to the fitting stage.

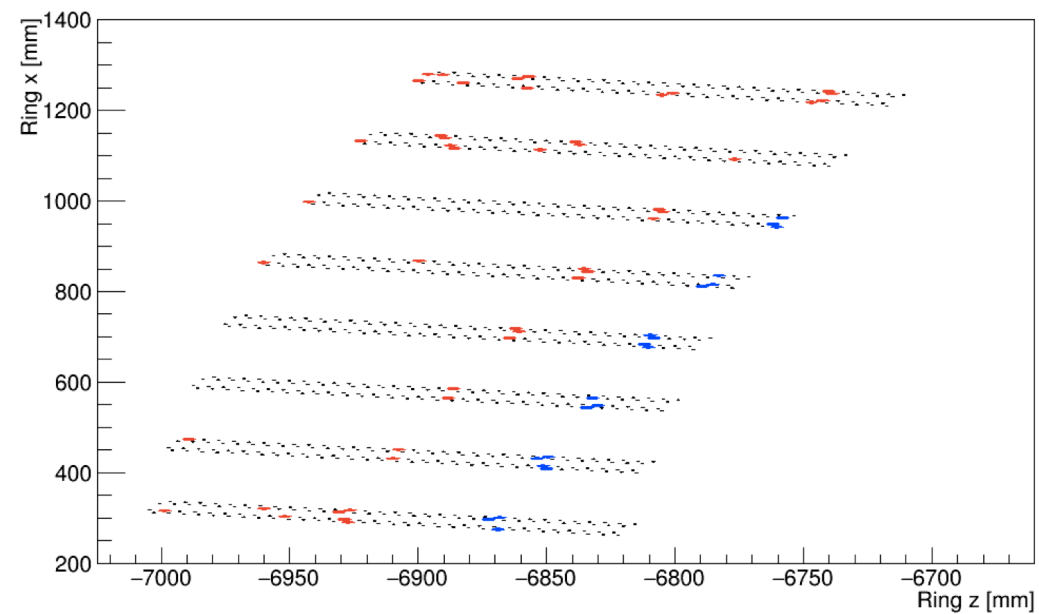


Figure 4·1: Hits in a tracker station in a single time island. The black dots indicate the position of the straws, while the blue and red points indicate hits. In blue is the first formed track candidate in the island, formed from separate seeds in different modules. The track finding algorithms will move onto the remaining hits in the time island to attempt to form other track candidates, one of which is easily observable by eye.

4.2 Track Fitting

The track fitting stage takes the track candidates from the track finding stage, and outputs a best fit trajectory to those candidates. This includes optimal state vectors and error matrices for the track at each measurement plane and at a fictitious starting plane at the entrance to the straw tracking detector. The track fitting routines can roughly be split into two parts, error propagation and the actual fitting and improvement of the track. The implementation of these parts go hand in hand, and will be described in turn.

4.2.1 Geometry and error propagation

To put it simply, the process of error propagation involves taking track parameters and error matrices (which describe the spread in those track parameters) and transporting them along discrete steps from one point to another, accounting for changes due to any present magnetic fields or material along the step path. There is a set of error propagation routines originally written in Fortran by the EMC collaboration, called “Geometry and Error Propagation” or Geane [58]. Geane works by propagating particles along their average trajectories neglecting the effects of discrete processes, using a helix equation along small enough steps where the change in the magnetic field is small. These routines were used in the E821 experiment as well as the PANDA experiment with some success [59]. The Geane routines were at one point converted to C++ and added to Geant4. The strength of using Geane within a Geant4 simulation lies in its direct access to the Geant4 geometry and field. This is crucially important for the E989 track fitting because the trackers live in a region of high field non-uniformity. Shown in Figure 4.2 is the location of the tracker with respect to the radial and vertical fields. As shown the radial field in the tracker region rises from 0 T at the outer ends to roughly 0.3 T at the inner top and bottom ends, and the vertical

field drops approximately 50% from the storage dipole field of 1.451 T. These large field gradients over the tracking measurement space must be handled appropriately, which Geane does nicely.

Predicted track parameters in Geane are a function of path length

$$p_l = F_{l,l_0}(p_0), \quad (4.1)$$

where p_0 are some original tracker parameters and p_l are the updated ones. The path length l can be defined or limited how one wishes, and typically correspond to a single step in the Geant4 simulation. The track parameter vectors p are defined in some coordinate system. In the Geane routines these track parameters are 5×1 vectors either defined in the “free” (curvilinear) system

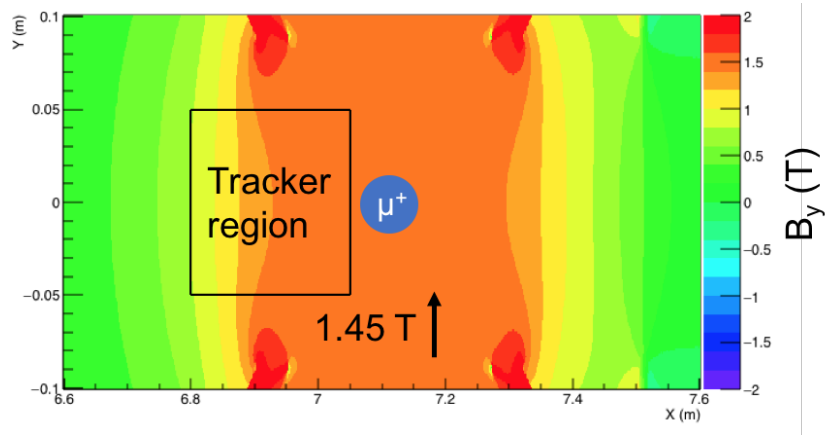
$$\frac{1}{p}, \lambda, \phi, y_\perp, z_\perp, \quad (4.2)$$

or the “surface” (detector) system

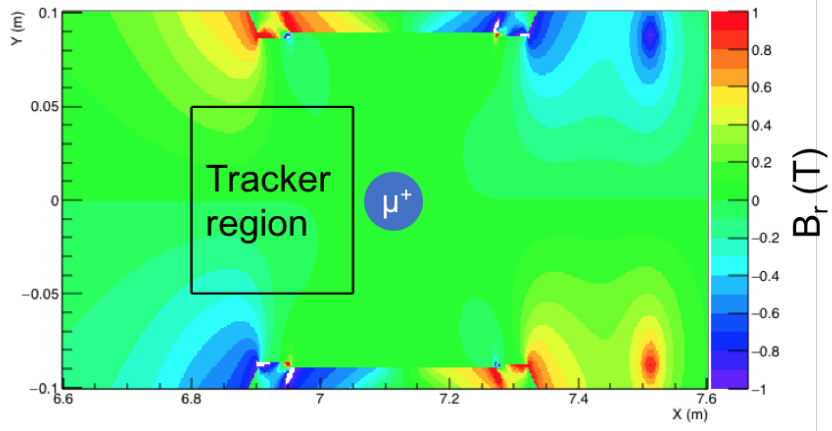
$$\frac{1}{p}, \frac{p_v}{p_u}, \frac{p_w}{p_u}, v, w. \quad (4.3)$$

In the free system, the λ and ϕ parameters are the dip ($\pi/2 - \theta$) and azimuthal angles respectively, while the y_\perp and z_\perp parameters are defined as being in the XY or XZ global Geant4 planes and orthogonal to x_\perp , where x_\perp is defined as being along the momentum vector of the particle. (Decide whether I want to try and supply a picture showing this here.) In the surface system, the UVW coordinates can be defined with any two orthogonal vectors V and W¹. The surface system is most usefully defined in the tracker reference frame, where the modules are staggered in a local Z coordinate, the local Y coordinate is vertical, and the local X coordinate increases with straw

¹For clarification, the UVW surface system has nothing to do with the UV orientations of the straws.



(a) Vertical magnetic field



(b) Radial magnetic field

Figure 4.2: Shown are the vertical (top) and radial (bottom) magnetic fields of the storage ring magnet in and around the storage region as calculated in Opera 2D. The horizontal and vertical axes are the radial and vertical coordinates of the ring respectively. The center of the storage region lies at 7.112 m along the horizontal axis. The contours represent the strengths of the vertical and radial magnetic fields. The black box shows the rough location of the tracker with respect to the ring. It can be seen that there is a large field non-uniformity within the tracker space.

number. See Figure 4.3. The surface system is then defined as

$$\frac{1}{p}, \frac{p_x}{p_z}, \frac{p_y}{p_z}, x, y. \quad (4.4)$$

In both free and surface cases the track is represented by one momentum parameter, two directional parameters, and two position parameters. Needing six independent parameters to describe a particle in space and momentum (three momentum and three position parameters), one parameter is left out and taken as a known variable. For Geane this is taken either as a known path length in the free system, or a known U coordinate in the surface system (or known Z coordinate in our tracker reference frame). In our tracker measurement frame, the 32 straw layers corresponding to a tracking station are defined at known Z coordinates in the tracker reference frame. The path lengths for steps in Geane can be set to be equal to the distance for a track to travel between between detector planes, and therefore the track parameter dependence on the path length can instead be replaced by a dependence on plane number.

The 5×5 error matrix on a plane calculated in Geane describing the expected distribution in true parameters about the average ones due to discrete process is defined as

$$\sigma^{ij} = \langle p^i p^j \rangle - \langle p^i \rangle \cdot \langle p^j \rangle, \quad (4.5)$$

where i and j are track parameter indices. This error matrix will include effects from multiple scattering, delta ray production, ionization, and bremsstrahlung [58, 60]. These matrices are transported from plane to plane through what are called transport matrices, where the 5×5 transport matrix elements between two planes

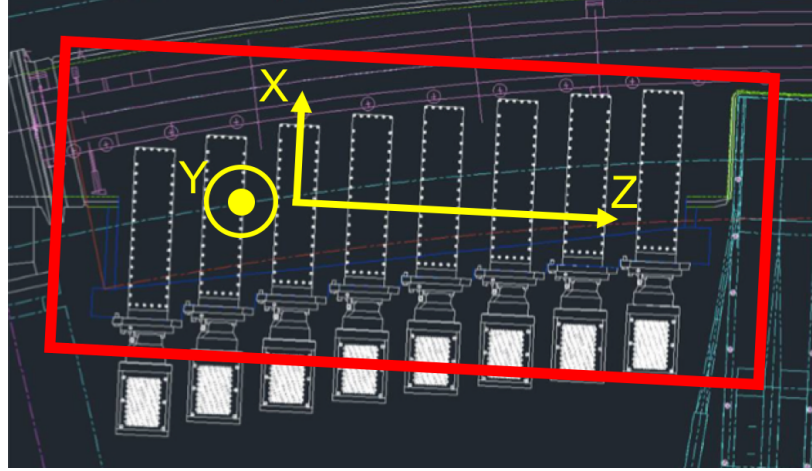


Figure 4.3: Shown is a model view of a tracker station in relation to the magnetic ring. Tracker modules are shown in white. Around the tracker measurement area is defined a coordinate system called the tracker reference frame. In that frame, the X coordinate is directed outward along the straws nearly radial, the Y coordinate is directed vertically up, and the Z coordinate is directed along the direction that the tracker modules are staggered.

are defined as

$$T_{N,N-1}^{i,j} = \frac{\partial p_N^i}{\partial p_{N-1}^j}, \quad (4.6)$$

where N is some plane number. The transport matrix T is simply a Jacobian matrix between planes. Therefore the error matrix propagated forward from one plane to another is given by

$$\sigma_N = T_{N,N-1} \sigma_{N-1} T_{N,N-1}^T + \sigma_{\text{material}}, \quad (4.7)$$

where σ_{material} is the added error due to material effects between the planes. Similarly, if there is some small change in track parameters on a plane, those small changes can be propagated forward to new changes on a later plane by

$$\delta p_N = T_{N,N-1} \delta p_{N-1}. \quad (4.8)$$

The calculation of the transport matrices themselves is done within the Geane routines in the free system, where the derivation of the transport matrix elements is given in Reference [61]. Geane can convert between the free system and the surface system using further Jacobians, also derived in Reference [61].

These parameter vectors are 5x1 objects defined in some track representation, as described in the Coordinate Systems section. The propagation of these parameters and error matrices are done using transport matrices, which express the infinitesimal changes in parameters at some plane (or path length) with respect to the parameters at some previous plane (or previous path length):

$$\delta p_N = T_{N,N-1} \delta p_{N-1}, \quad (4.9)$$

$$\sigma_N = T_{N,N-1} \sigma_{N-1} T_{N,N-1}^T. \quad (4.10)$$

Said transport and error matrices are 5x5 objects since the parameter vectors are 5x1 objects as described above. The calculation of these transport matrices, as well as details on the functional form of 4.1 are shown in [61].

As Geane propagates particles along their average trajectories,

The transformation between the free and surface systems is done by applying a Jacobian transformation - this only applies to matrices though...

the transformation between the two is handled in the code and given by reference

..

Geane does everything in the free system and converts to the surface system ...

transport matrices are calculated in ...

step by step vs plane by plane

inverse vs transpose

-it was found that doing the minimization in UV space removed correlations (cite James here) instead of XY

-need to see what I've written down below, and what I might move up here and such

-average path -helix -cite proper stuff

-need to talk about material effect calculations -reference frames and multiplica-

tion of matrices to go between them -transport and error matrix calculations -eq 4.5
not quite right

measurement error being the largest error ...

-don't forget to cite my track fitting note probably

4.2.2 χ^2 minimization

-globabl chi2 minimization -other fitting algortihms could be used, kalman filter by lavezzi

I recommend reading [58], Chapter 4 of [59], and [62] in order to best understand the fitting algorithm. However, due to the at times confusing notation, ommitted equations or concepts, and differences between papers, I have attempted to summarize here the different sources and present the material in a more understandable and readable format. The implementation of the fitting algorithm into the code follows this section.

One can define a χ^2 for a track in the usual way by dividing the residuals of measured and predicted track parameters by their errors:

$$\chi^2 = (\vec{p} - \vec{x})^T (\sigma^{-1}) (\vec{p} - \vec{x}), \quad (4.11)$$

where \vec{p} are predicted track parameters from a fit to the measured track parameters \vec{x} , and σ is a covariance matrix of errors on the fitted parameters. The Geant4 error propagation routines can be used to determine these predicted parameters and error matrices by propagating track parameters from some initial guesses. By minimizing this χ^2 with respect to the track parameters one can then fit and improve the track.

With parameters defined on such planes, one can define the χ^2 as:

$$\chi^2 = \sum_{i=1}^N [(p_i(p) - x_i)^T (\sigma_i^{-1}) (p_i(p) - x_i)], \quad (4.12)$$

where p_i are the average predicted parameters from some general starting parameters p . At first order one can solely include the measurement errors on parameters, which fill in the diagonals of σ_i , if random processes can be neglected. Unmeasured parameters should have measurement errors of infinity (or some large value) along the diagonals in the code, which account for the fact that residuals for unmeasured parameters do not exist. When the error matrix is inverted all rows and columns of the matrix with these large numbers will fall to 0 in the χ^2 .

In order to get the best fit track, the χ^2 should be minimized with respect to the initial track parameters p , and evaluated at some chosen or fitted parameters:

$$\frac{\partial \chi^2}{\partial p} \Big|_{p=p'_0} = 0, \quad (4.13)$$

resulting in

$$\begin{aligned} 0 = & \sum_{i=1}^N \left[\left(\frac{\partial p_i(p)}{\partial p} \Big|_{p=p'_0} \right)^T (\sigma_i^{-1}) (p_i(p'_0) - x_i) \right. \\ & + (p_i(p'_0) - x_i)^T \frac{\partial (\sigma_i^{-1})}{\partial p} \Big|_{p=p'_0} (p_i(p'_0) - x_i) \\ & \left. + (p_i(p'_0) - x_i)^T (\sigma_i^{-1}) \left(\frac{\partial p_i(p)}{\partial p} \Big|_{p=p'_0} \right) \right] \end{aligned} \quad (4.14)$$

where the 1st and 3rd terms are identical, and the 2nd term is small if one assumes that the error matrix doesn't change much with respect to the starting parameters. (Fair since most of the error comes from measurement, and as long as the initial guess is decent enough such that the path length through material doesn't change appreciably from one iteration to the next.) This simplifies to:

$$\sum_{i=1}^N T_{i0}^T (\sigma_i^{-1}) (p_i(p'_0) - x_i) = 0, \quad (4.15)$$

which is just the top term with

$$T_{i0} = \frac{\partial p_i(p)}{\partial p}. \quad (4.16)$$

To solve this make the substitution

$$p_i(p'_0) = p_i(p_0) + \frac{\partial p_i(p_0)}{\partial p} \Delta p_0 = p_i(p_0) + T_{i0} \Delta p_0, \quad (4.17)$$

where p'_0 are the improved starting parameters for the next iteration calculated from the previous starting parameters p_0 , and Δp_0 are the changes in the starting parameters to improve the track. This equation can be plugged into the above if one makes the assumption that T_{i0} does not change much from one iteration to the next, which follows from the inherent nature of making small adjustments to the track in order to improve it.

After simplifying one arrives at

$$\Delta p_0 = \sigma_{p_0} \sum_{i=1}^N T_{i0}^T (\sigma_i^{-1}) (x_i - p_i(p_0)), \quad (4.18)$$

where

$$\sigma_{p_0} = \left[\sum_{i=1}^N T_{i0}^T (\sigma_i^{-1}) T_{i0} \right]^{-1}, \quad (4.19)$$

is the 5x5 covariance matrix of fitted parameters on the starting plane, whose diagonals describe the errors in the 5 track parameters on that plane and in the region close to it. (The fit does not directly return fit errors for track parameters on other planes.) Δp_0 along with χ^2 is exactly what we want to determine since that is what allows us to fit and improve the track from iteration to iteration.

However, since random processes should not be neglected for optimal tracking results, it makes more sense to return to the original χ^2 in equation 4.11, only now

the included matrix and vector objects are combined into one large linear algebra equation. Instead of a sum over N 5x1 objects multiplying 5x5 error matrices, the vectors are combined into a single 5Nx1 vector multiplying a single 5Nx5N matrix. The 5x5 diagonal blocks of this large error matrix should now include the effects due to material processes as calculated in Geant from equation 4.5 as well as the measurement errors.

Because now parameters at one plane are no longer independent of the parameters at other planes, due to correlations from these random processes, it's necessary to add off-diagonal elements into the large error matrix. These 5x5 blocks come from

$$\sigma_{MN} = T_{MN}\sigma_N, \quad (4.20)$$

for the top diagonals, and the transpose for the bottom diagonals, where M and N are two separate planes within the detector. (σ_N is the error matrix on plane N calculated from the starting plane.) This follows from equation 4.5 evaluated at plane M with respect to a path length from plane N, and not plane 0, which is equivalent to 4.20.

You can then minimize the χ^2 in the same way, only again with the matrix objects being aggregates of the per plane objects:

$$\Delta\vec{p}_0 = \sigma_{p_0}\tau^T\sigma^{-1}(\vec{x} - \vec{p}), \quad (4.21)$$

$$\sigma_{p_0} = [\tau^T\sigma^{-1}\tau]^{-1}, \quad (4.22)$$

where τ is the combined transport matrices from the individual 5x5 matrices, a 5Nx5 object.

The unmeasured parameter errors of infinity still come into play in the final calculation in the same was as before. Because however these matrix objects are very large, and the tracking must have a certain amount of speed in order to keep up with

data, it is useful to reduce the size of these matrices. (It also makes things easier programming wise. Note that there are other some other ways to speed things up, specifically the banded inversion method as described in reference [62]. This method was not used in favor of getting the code working in the simpler form in the first place, but it is a possibility in the future to use this technique to speed things up even more.) It suffices to simply remove all rows and columns where said infinity values exist in the error matrix. This is mathematically equivalent to inverting the error matrix with the infinities included, which make all rows and columns where they exist go to zero. The associated unmeasured parameter rows in the residual vector and transport matrices must similarly be removed. This results in an Nx1 residual vector, NxN error matrix, 5xN combined transport matrix transpose, which multiply against the 5x5 covariance matrix out front to still result in a 5x1 fix to the starting parameters, and a scalar χ^2 value. (Note that these element removals should be done just before the final calculation, and not higher up in the algebra, otherwise plane correlations are not properly calculated.)

By calculating the last two equations one can fit the track, acquire a χ^2 describing the degree of the fit, determine how the track parameters can be improved at the starting point, and calculate errors on those starting parameters. This algorithm can be iterated a number of times to get a best fit track until successive iterations produce no improvement, where usually 3 or 4 iterations is enough. Note that there is remarkable robustness with respect to the initial starting parameters in fitting the track. Of course if the initial starting parameters are too poor, then the fit will not converge. All of these calculations are completed within the GeaneFitter.cc file within the framework.

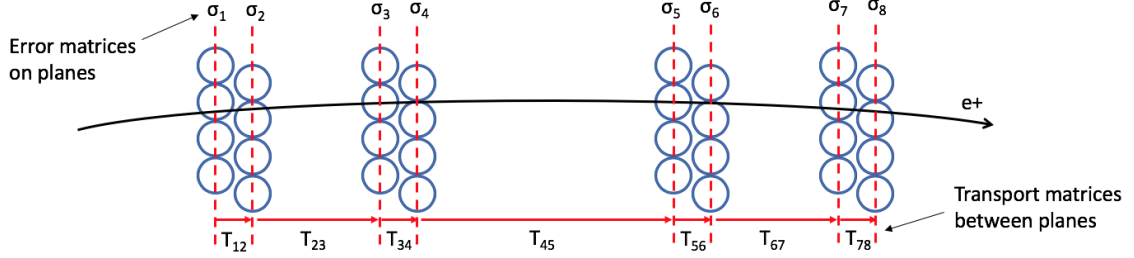


Figure 4.4

4.2.3 Left right ambiguity

-go into all tests and pieces of the code -vacuum fitting -checks on energy loss -material correlation code -fast fitting code -different fitting modes -mc / data comparisons - don't forget about angular correction in appendix of fitting documentation - might want to put that in the appendix of my thesis -red black point residual plots too maybe -talk about the dummy stuff too perhaps -fictitious starting plane

-should talk about geometry determination of hits in straws which I havent yet - in the fitting side of things though - see Joes docdb 6947 to start (maybe others too) - for LR determination after wire fit (but only in full sequence fit I believe...)

4.3 Track Extrapolation

The last stage of the track reconstruction is the track extrapolation. The extrapolation takes the fitted track results and either extrapolates them back to the storage region to the approximate position of the muon decay point, or forwards to the face of the calorimeter sitting right behind the tracker. The extrapolation stage utilizes a fourth order Runge-Kutta Nyström algorithm [51] which discretely steps a trajectory through the magnetic field in the full $g - 2$ Geant4 simulation, similar in some respects to the track fitting stage. At each step of the extrapolation, the updated track position and covariance matrix are compared to physical volumes in the simulation to flag tracks which have been reconstructed as likely originating from outside the

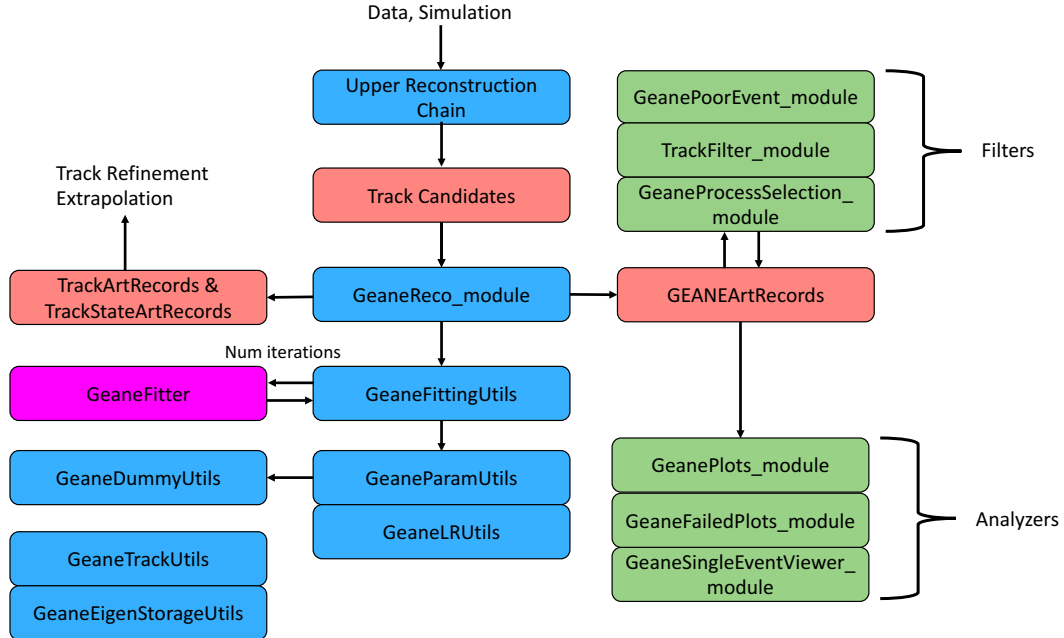


Figure 4.5

storage region [51, 63]. Because there is no fixed interaction point in the storage region, tracks are extrapolated backwards to the point of tangency where the radial momentum is equal to zero. Studies were done to verify that this approximation for the muon decay point was sufficient using truth Monte-Carlo, and it was found that a simple 1.1 mm correction to the radial decay position could be applied regardless of the momentum of the track [51]. The vertical extrapolated distribution was found to have no biases. (What about the azimuthal point? Mentioned a little bit in DocDB 8564 but do I really want to go into it?) A birds eye view for extrapolation results is shown in Figure 4.6. A radial slice of the extrapolated beam distribution is shown in Figure 4.7.

4.4 Muon Beam Measurements

-for showing plots include a bulleted list or table of the tracking cuts made
 -emphasize measurements that are directly relevant to the calorimeter ω_a analysis

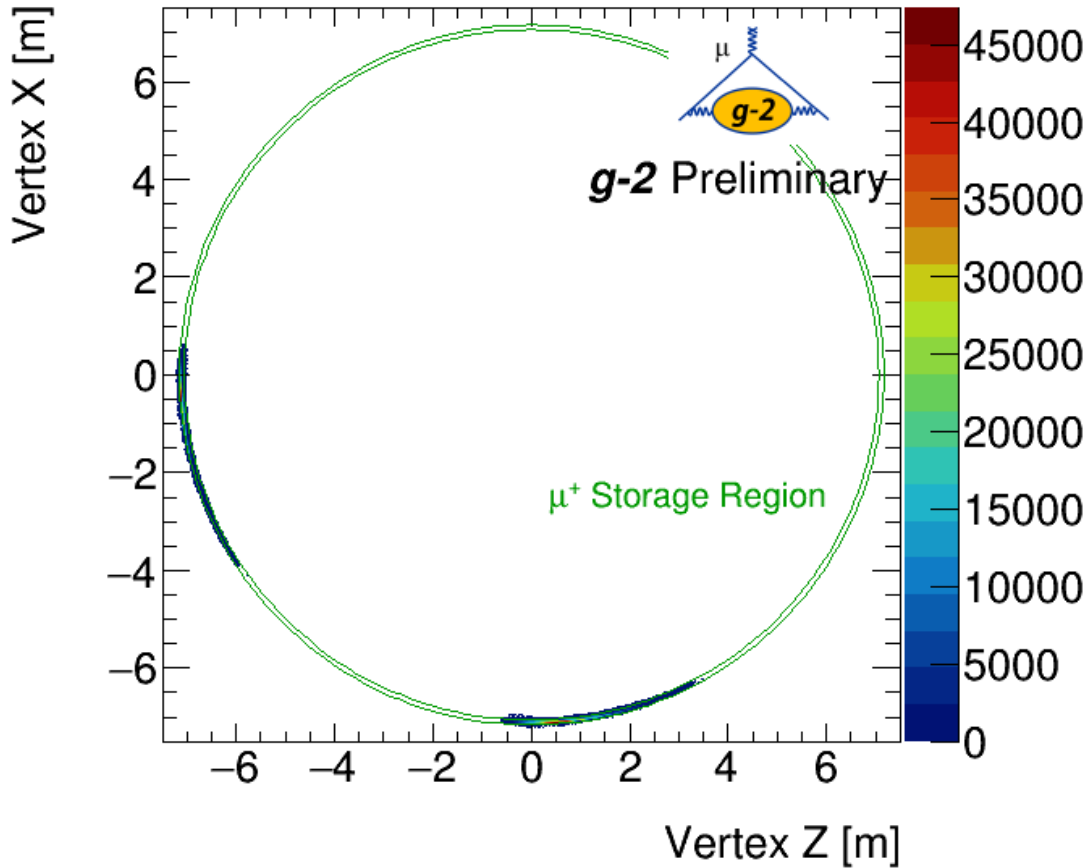


Figure 4·6: A birds eye view of the extrapolation results in the storage ring. The two distributions of extrapolated tracks can be seen at the left and bottom of the figure, where the tracker sits at the heads of the distributions. It can be seen that some tracks are extrapolated multiple meters back through the storage region. (Mention anything about the cuts in this plot?)

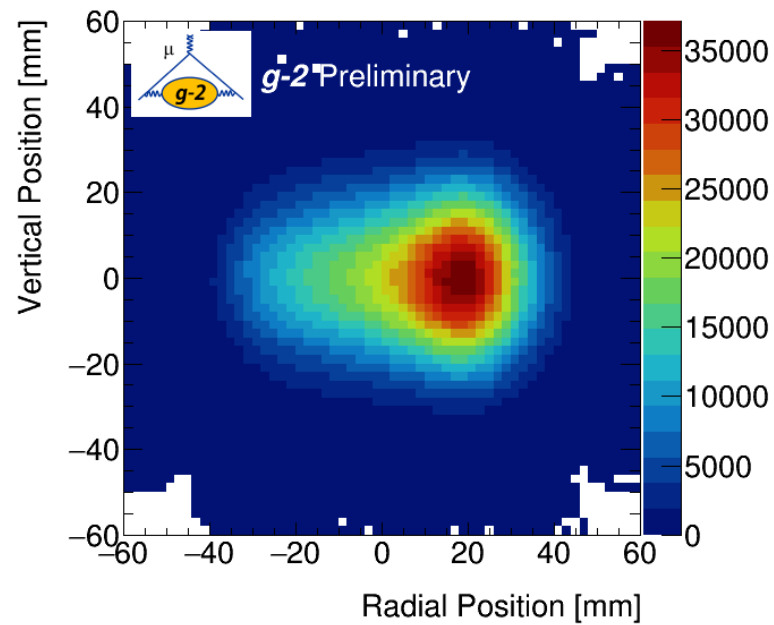


Figure 4.7: Shown is a radial slice of the extrapolated muon distribution or beam spot. The beam is localized off center of the storage ring due to the kicker settings used, Section 2.5.1. (Mention that last bit at all? Mention anything about the cuts in this plot?)

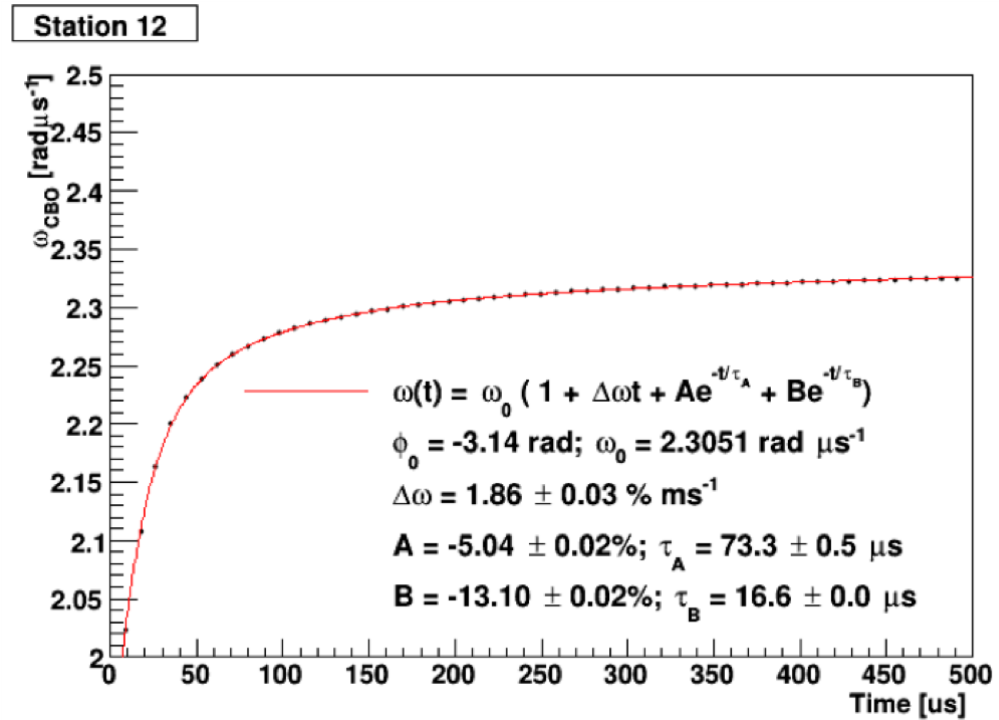


Figure 4.8

-cbo frequency -cbo amplitude -have a CBO subsection alongside general results?

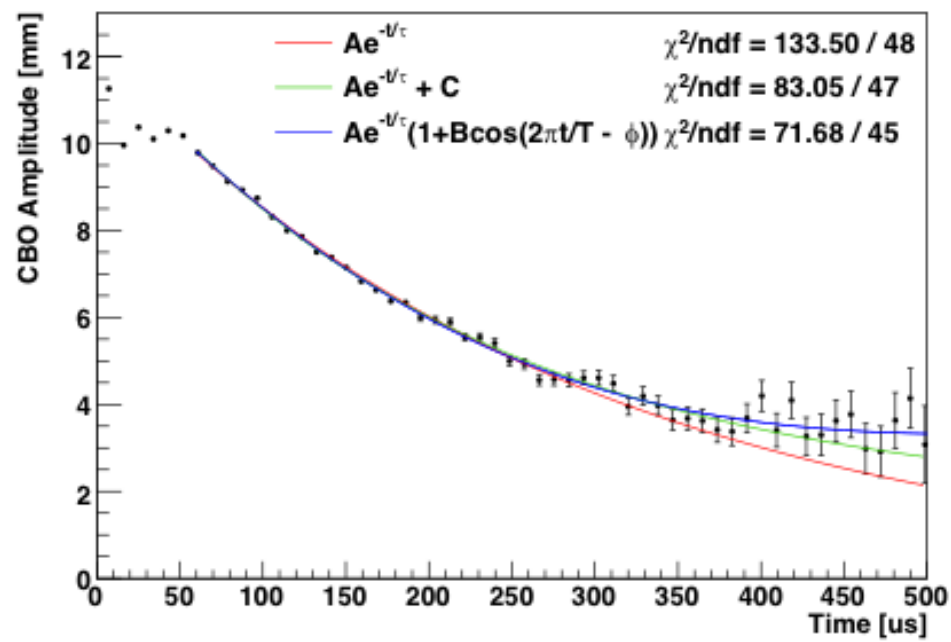


Figure 4.9

-in all pictures of this chapter (and others too), make sure to go back through figures and check that I've given credit properly

Chapter 5

ω_a Measurement

5.1 Details of Run 1

5.2 Reconstruction

[64]

5.2.1 Clustering

5.3 Histogramming

5.4 Fitting

5.5 Systematic Errors

Chapter 6

Conclusion

6.1 Run 1 value of a_μ

test4

Appendix A

g for Spin-1/2 Particles

Do I even want to include this derivation? Needs work if I am to do so. (If I remove it remove the reference in chapter 1 and just reference schwartz directly.)

Here is provided a relatively straightforward calculation of the g-factor for spin-1/2 particles, simplified from a derivation by Schwartz [65]. Start with the Dirac equation in the presence of an external electromagnetic field:

$$(i\gamma^\mu \partial_\mu - m - e\gamma^\mu A_\mu)\psi = 0, \quad (\text{A.1})$$

where ψ is the wavefunction of a spin-1/2 particle, m is its mass, A_μ is the electromagnetic field operator, ∂_μ is the 4-gradient, and γ^μ are the gamma matrices¹. Multiplying Equation A.1 by itself but with the sign on m switched, one arrives at the equation

$$[(i\partial_\mu - eA_\mu)(i\partial_\nu - eA_\nu)\gamma^\mu\gamma^\nu - m^2]\psi = 0. \quad (\text{A.2})$$

This can be split this into its symmetric and antisymmetric parts,

$$\left(\frac{1}{4}\{i\partial_\mu - eA_\mu, i\partial_\nu - eA_\nu\}\{\gamma^\mu, \gamma^\nu\} + \frac{1}{4}[i\partial_\mu - eA_\mu, i\partial_\nu - eA_\nu][\gamma^\mu, \gamma^\nu] - m^2 \right) \psi = 0, \quad (\text{A.3})$$

where $[,]$ and $\{, \}$ stand for the commutator and anti-commutator relations respec-

¹Here \hbar and c will be set equal to 1.

tively. Using the identities

$$\frac{i}{2}[\gamma^\mu, \gamma^\nu] = \sigma^{\mu\nu} \quad (\text{A.4})$$

and

$$[i\partial_\mu - eA_\mu, i\partial_\nu - eA_\nu] = -ie[\partial_\mu A_\nu - \partial_\nu A_\mu] = -ieF_{\mu\nu}, \quad (\text{A.5})$$

where $\sigma^{\mu\nu}$ is a tensor with elements consisting of the Pauli matrices, and $F_{\mu\nu}$ is the electromagnetic field tensor, Equation A.3 can be formed as

$$((i\partial_\mu - eA_\mu)^2 - \frac{e}{2}F_{\mu\nu}\sigma^{\mu\nu} - m^2)\psi = 0. \quad (\text{A.6})$$

Expanding out the tensor objects

$$\frac{e}{2}F_{\mu\nu}\sigma^{\mu\nu} = -e \begin{pmatrix} (\vec{B} + i\vec{E}) \cdot \vec{\sigma} & 0 \\ 0 & (\vec{B} - i\vec{E}) \cdot \vec{\sigma} \end{pmatrix} \quad (\text{A.7})$$

and forming a new covariant derivative

$$\not{D}^2 = D_\mu^2 + \frac{e}{2}F_{\mu\nu}\sigma^{\mu\nu} \quad (\text{A.8})$$

where $D_\mu = \gamma^\mu\partial_\mu$ is your ordinary covariant derivative, by moving to momentum space (this part is awkward) you can arrive at the equation

$$\frac{(H + eA)^2}{2m}\psi = \left(\frac{m}{2} + \frac{(\vec{p} + e\vec{A})^2}{2m} - 2\frac{e}{2m}\vec{B} \cdot \vec{s} \pm i\frac{e}{m}\vec{E} \cdot \vec{s}\right)\psi. \quad (\text{A.9})$$

Lo and behold, you have arrived at the Dirac $g = 2$ result, contained in front of the magnetic piece in the form of Equation ??.

How then does such a term change at loop level? Most generally the vertex of a particle interacting with a magnetic field through the mediation of a photon can be

represented by

$$iM^\mu = \bar{u}(q_2)(f_1\gamma^\mu + f_2p^\mu + f_3q_1^\mu + f_4q_2^\mu)u(q_1) \quad (\text{A.10})$$

where q_1 and q_2 are the ingoing and outgoing four-momenta respectively, which can be constrained on-shell, and p is the four-momenta of the photon, which is off-shell. The f_i are in general contractions of four-momenta and gamma matrices. By using the Gordon identity

$$\begin{aligned} & \bar{u}(q_2)(q_1^\mu + q_2^\mu)u(q_1) \\ &= (2m)\bar{u}(q_2)\gamma^\mu u(q_1) + i\bar{u}(q_2)\sigma^{\mu\nu}(q_1^\nu - q_2^\nu)u(q_1) \end{aligned} \quad (\text{A.11})$$

any Feynman diagram can be reorganized into the form

$$iM^\mu = (-ie)\bar{u}\left[F_1\left(\frac{p^2}{m^2}\right)\gamma^\mu + \frac{i\sigma^{\mu\nu}}{2m}p_\nu F_2\left(\frac{p^2}{m^2}\right)\right]u, \quad (\text{A.12})$$

where F_1 and F_2 are form factors. One notices that the F_2 piece is reminiscent of our magnetic dipole moment form that we derived from the Dirac equation. So the problem now becomes for any Feynman diagram calculation in any theory, at any order, to solve for this F_2 to determine the contribution to the magnetic dipole moment.

Appendix B

Ratio Method Derivation

B.1 Ratio form and function

Consider the 5 parameter function:

$$N_5(t) = N_0 e^{-t/\tau} (1 + A \cos(\omega_a t + \phi)), \quad (\text{B.1})$$

which describes some ideal dataset in histogram format. Here ϕ will be set to zero for simplicity. Now define the variables $u_+(t)$, $u_-(t)$, $v_1(t)$, and $v_2(t)$ as

$$\begin{aligned} u_+(t) &= \frac{1}{4} N_5(t + T/2) \\ u_-(t) &= \frac{1}{4} N_5(t - T/2) \\ v_1(t) &= \frac{1}{4} N_5(t) \\ v_2(t) &= \frac{1}{4} N_5(t), \end{aligned} \quad (\text{B.2})$$

where the $1/4$ out front reflects randomly splitting the whole dataset into 4 equally weighted sub-datasets, and T is the g-2 period known to high precision, $\mathcal{O}(10^{-6})$. This corresponds to a weighting of 1:1:1:1 between the datasets. To be explicit here regarding the signs, the counts that are filled into the histogram described by u_+ have their times shifted as $t \rightarrow t - T/2$, which is what the function $N_5(t + T/2)$ describes,

and vice versa for u_- . To form the ratio define the variables:

$$\begin{aligned} U(t) &= u_+(t) + u_-(t) \\ V(t) &= v_1(t) + v_2(t) \\ R(t) &= \frac{V(t) - U(t)}{V(t) + U(t)}. \end{aligned} \tag{B.3}$$

Plugging in and dividing the common terms ($N_0 e^{-t/\tau}/4$),

$$R(t) = \frac{2(1 + A \cos(\omega_a t)) - e^{-T/2\tau}(1 + A \cos(\omega_a t + \omega_a T/2)) - e^{T/2\tau}(1 + A \cos(\omega_a t - \omega_a T/2))}{2(1 + A \cos(\omega_a t)) + e^{-T/2\tau}(1 + A \cos(\omega_a t + \omega_a T/2)) + e^{T/2\tau}(1 + A \cos(\omega_a t + \omega_a T/2))}. \tag{B.4}$$

Now set $\omega_a T/2 = \delta$, and note that T is really

$$\begin{aligned} T &= T_{guess} = \frac{2\pi}{\omega_a} + \Delta T, \\ \Delta T &= T_{guess} - T_{true}. \end{aligned} \tag{B.5}$$

Being explicit,

$$\delta = \frac{\omega_a}{2} T_{guess} = \frac{\omega_a}{2} \left(\frac{2\pi}{\omega_a} + \Delta T \right) = \pi + \pi \frac{\Delta T}{T_{true}} = \pi + \pi(\delta T), \tag{B.6}$$

and δ can be redefined as

$$\delta = \pi(\delta T), \tag{B.7}$$

by flipping the sign of any cosine terms that contain δ .

Then, using the trig identity

$$\cos(a \pm b) = \cos(a) \cos(b) \mp \sin(a) \sin(b) \tag{B.8}$$

so that

$$\begin{aligned}
\cos(\omega_a t \pm \delta) &= \cos(\omega_a t) \cos \delta \mp \sin(\omega_a t) \sin \delta \\
&\approx \cos(\omega_a t)(1 - \delta^2) \mp \sin(\omega_a t)\delta \\
&\approx \cos(\omega_a t),
\end{aligned} \tag{B.9}$$

since $\delta \sim O(10^{-5})$, the ratio becomes

$$R(t) \approx \frac{2(1 + A \cos(\omega_a t)) - (1 - A \cos(\omega_a t))(e^{-T/2\tau} + e^{T/2\tau})}{2(1 + A \cos(\omega_a t)) + (1 - A \cos(\omega_a t))(e^{-T/2\tau} + e^{T/2\tau})}. \tag{B.10}$$

Expanding

$$e^{\pm T/2\tau} = 1 \pm \frac{T}{2\tau} + \frac{1}{2} \left(\frac{T}{2\tau} \right)^2 \pm \dots, \tag{B.11}$$

replacing and simplifying,

$$R(t) \approx \frac{A \cos(\omega_a t) - C(1 - A \cos(\omega_a t))}{1 + C(1 - A \cos(\omega_a t))}, \tag{B.12}$$

where

$$C = \frac{1}{16} \left(\frac{T}{\tau} \right)^2 \approx 2.87 * 10^{-4}. \tag{B.13}$$

Using the expansion

$$f(x) = \frac{1}{1+x} = 1 - x + x^2 - \dots, \quad |x| < 1, \tag{B.14}$$

and since C is small, the denominator can be manipulated such that

$$\begin{aligned}
R(t) &\approx (A \cos(\omega_a t)) - C(1 - A \cos(\omega_a t))(1 - C(1 - A \cos(\omega_a t))) \\
&\approx A \cos(\omega_a t) - C + CA^2 \cos^2(\omega_a t),
\end{aligned} \tag{B.15}$$

after dropping terms of $\mathcal{O}(C^2)$ and higher. In practice the last term is omitted since

it has a minimal effect on the fitted value of ω_a [cite], and one arrives at

$$R(t) \approx A \cos(\omega_a t) - C, \quad (\text{B.16})$$

the conventional 3 parameter ratio function.

In order to avoid approximations one can instead weight the counts in the histograms as

$$u_+(t) : u_-(t) : v_1(t) : v_2(t) = e^{T/2\tau} : e^{-T/2\tau} : 1 : 1, \quad (\text{B.17})$$

so that

$$\begin{aligned} u_+(t) &= \frac{e^{T/2\tau}}{2 + e^{T/2\tau} + e^{-T/2\tau}} N_5(t + T/2) \\ u_-(t) &= \frac{e^{-T/2\tau}}{2 + e^{T/2\tau} + e^{-T/2\tau}} N_5(t - T/2) \\ v_1(t) &= \frac{1}{2 + e^{T/2\tau} + e^{-T/2\tau}} N_5(t) \\ v_2(t) &= \frac{1}{2 + e^{T/2\tau} + e^{-T/2\tau}} N_5(t). \end{aligned} \quad (\text{B.18})$$

(These factors out front aren't so far off from 1/4 since $e^{\pm T/2\tau} \approx e^{\pm 4.35/2*64.4} \approx 1.034, .967$.) Then instead $R(t)$ becomes

$$R(t) = \frac{2(1 + A \cos(\omega_a t)) - (1 - A \cos(\omega_a t + \delta)) - (1 - A \cos(\omega_a t - \delta))}{2(1 + A \cos(\omega_a t)) + (1 - A \cos(\omega_a t + \delta)) + (1 - A \cos(\omega_a t - \delta))}, \quad (\text{B.19})$$

where the $e^{\pm T/2\tau}$ terms out front now cancel. Using Equation B.9 again and this time avoiding approximations in δ ,

$$R(t) = \frac{2A \cos(\omega_a t)(1 + \cos \delta)}{4 + 2A \cos(\omega_a t)(1 - \cos \delta)}, \quad (\text{B.20})$$

after simplifying. In the limit that

$$\delta = \pi(\delta T) \rightarrow 0 \quad (\text{B.21})$$

since δT is small,

$$R(t) \approx A \cos(\omega_a t), \quad (\text{B.22})$$

with the only approximation being made at $\mathcal{O}(\delta^2) \sim \mathcal{O}(10^{-10})$.

Finally, while the 3 parameter ratio function suffices for fits to data containing slow modulations, it does not suffice for faster oscillation features. In that case it is more useful to fit with the non-approximated or simplified version of the ratio,

$$\begin{aligned} R(t) &= \frac{v_1(t) + v_2(t) - u_+(t) - u_-(t)}{v_1(t) + v_2(t) + u_+(t) + u_-(t)}, \\ &= \frac{2f(t) - f_+(t) - f_-(t)}{2f(t) + f_+(t) + f_-(t)}, \end{aligned} \quad (\text{B.23})$$

where

$$\begin{aligned} f(t) &= C(t)(1 + A \cos(\omega_a t + \phi)) \\ f_{\pm}(t) &= f(t \pm T_a/2), \end{aligned} \quad (\text{B.24})$$

and $C(t)$ can encode any other effects in the data that need to be fitted for, such as the CBO,

$$C(t) = 1 + A_{cbo} \cdot e^{-t/\tau_{cbo}} \cdot \cos(\omega_{cbo}t + \phi_{cbo}). \quad (\text{B.25})$$

Additionally, any other fit parameters such as A or ϕ can be made a function of t . Using the non-approximated form for the final fit function gives greater confidence in the fit results for the high precision ω_a extraction necessary for the experimental measurement.

B.2 Ratio errors

In order to determine the errors on the points in the formed ratio, Equation B.3, we use standard error propagation:

$$\sigma_R(t)^2 = \left(\frac{\partial R(t)}{\partial V(t)} \right)^2 \delta V(t)^2 + \left(\frac{\partial R(t)}{\partial U(t)} \right)^2 \delta U(t)^2 \quad (\text{B.26})$$

This works because $V(t)$ and $U(t)$ are statistically independent datasets. Using standard error propagation again,

$$\begin{aligned} \delta V(t)^2 &= \delta v_1(t)^2 + \delta v_2(t)^2 = v_1(t) + v_2(t) = V(t), \\ \delta U(t)^2 &= \delta u_+(t)^2 + \delta u_-(t)^2 = u_+(t) + u_-(t) = U(t). \end{aligned} \quad (\text{B.27})$$

Calculating out and simplifying the partial derivatives, (and this time dropping the t 's),

$$\begin{aligned} \frac{\partial R}{\partial V} &= \frac{2U}{(V+U)^2}, \\ \frac{\partial R}{\partial U} &= \frac{-2V}{(V+U)^2}. \end{aligned} \quad (\text{B.28})$$

Combining and simplifying, we arrive at the error formula:

$$\sigma_R^2 = \frac{4UV}{(V+U)^3} = \frac{1-R^2}{(V+U)} \quad (\text{B.29})$$

Appendix C

Pileup Modified Errors

In the pileup subtraction method detailed in Section ??, pileup events are statistically constructed and then subtracted from the data. Because of this, the errors on the bins need to be adjusted appropriately. Reference [66] describes the modified errors, but is not quite correct. Here is provided an improved calculation that I believe is easier to understand. While we are mainly interested in the errors on the histogram bins after pileup subtraction, it first helps to examine the errors of the pileup histogram itself. Here we only consider doublets.

In the asymmetric shadow window pileup method, shadow doublets are constructed from two singlets. The pileup histogram is then filled as the sum of the doublets minus the singlets,

$$P = D - S, \tag{C.1}$$

where D or S are only added or subtracted when they are above some energy threshold. If the threshold is set to 0, then for every doublet one entry will be added and two will be subtracted. Since these entries are exactly correlated, the error in each time bin will be

$$\sigma_P = \sqrt{N_D}, \tag{C.2}$$

where N_D is the number of doublets in that time bin. If the energy threshold is above 0, then we can determine whether the counts in the pileup histogram increase

	$E_1 < E_{th}$	$E_1 > E_{th}$
$E_2 < E_{th}$	$N_1(+1)$	$N_2(0)$
$E_2 > E_{th}$	$N_3(0)$	$N_4(-1)$

Table C.1: Table of doublets above threshold. Here E_1 and E_2 are the energies of the two singlets, E_{th} is the energy threshold, and N_i are the number of doublets above threshold for the different combinations of E_1 and E_2 . (N_1 is assumed above threshold here.) The numbers in the parentheses indicate the number of counts gained or lost in the pileup histogram.

or decrease based on whether the singlets and doublets are above threshold or not.

Table C.1 shows the different combinations of counts put into the pileup histogram.

The counts that go into P will be

$$\begin{aligned}
 P &= \sum_i N_i - \text{singlets above threshold} \\
 &= (N_1 + N_2 + N_3 + N_4) - (N_2 + N_4) - (N_3 + N_4) \\
 &= N_1 - N_4
 \end{aligned} \tag{C.3}$$

and the errors are

$$\sigma_P = \sqrt{N_1 + N_4}. \tag{C.4}$$

This makes sense considering the cases individually. In the cases for N_1 , you will gain a count from the doublet above threshold, and lose no counts since both singlets are below threshold. In the cases for N_2 and N_3 , you will gain a count from the doublet, and lose a count from one of the singlets which is above threshold. In the cases for N_4 , you will gain a count from the doublet and lose two counts from the singlets which are both above threshold. Since the doublet and singlets are exactly correlated, the N_1 and N_4 cases naturally result in a single weight being added into the error, while the N_2 and N_3 cases result in no additions to the error.

Now what about the pileup subtracted time spectrum? Our corrected spectrum can be written as

$$N_{\text{corrected}} = N_{\text{measured}} - P. \quad (\text{C.5})$$

What is in N_{measured} doesn't matter exactly. What we care about is what is in N_{measured} that is also within P , for that is where the correlations come from. Since N_{measured} is the sum of all singlets above threshold, we can write it as

$$N_{\text{measured}} = N_{\text{other}} + N_2 + N_3 + 2N_4 \quad (\text{C.6})$$

since we know that those cases N_i listed come from singlets above threshold, and N_{other} is anything in the measured hits that was not included in the pileup shadow construction. We can then replace P and simplify to get

$$N_{\text{corrected}} = N_{\text{other}} - N_1 + N_2 + N_3 + 3N_4. \quad (\text{C.7})$$

The error on the corrected histogram is then

$$\sigma_{N_{\text{corrected}}} = \sqrt{N_{\text{other}} + N_1 + N_2 + N_3 + 9N_4}. \quad (\text{C.8})$$

Replacing N_{other} as

$$N_{\text{other}} = N_{\text{corrected}} + N_1 - N_2 - N_3 - 3N_4, \quad (\text{C.9})$$

we can remove the dependence of the corrected histogram errors on the unknown quantity and arrive at

$$\begin{aligned} \sigma_{N_{\text{corrected}}} &= \sqrt{N_{\text{corrected}} + 2N_1 + 6N_4}, \\ &= \sqrt{N_{\text{corrected}}} \cdot \sqrt{1 + (2N_1 + 6N_4)/N_{\text{corrected}}}. \end{aligned} \quad (\text{C.10})$$

(This argument might seem circular at the end, but it works because of the squaring that occurs when calculating the error.) In the end we have a form for the bin errors of the pileup corrected histogram which only depend on N_1 and N_4 in addition to the number of counts in the corrected histogram. As shown it can be refactored into a form equal to the naive errors (just the bin content) times some correction factor. Since N_1 and N_4 are much smaller than $N_{\text{corrected}}$ at all times, and because they decay away at about twice the rate as the pileup diminishes, the change to the errors is small, of the order 1 or 2% at 30 μs .

C.1 Pileup errors for the ratio function

Equation C.10 applies to the corrected errors for a pileup subtracted histogram, but what about the modifications to the ratio errors? If we parameterize that equation as

$$\sigma_{N_{\text{corrected}}} = \sqrt{N_{\text{corrected}}} \cdot \sqrt{\gamma(t)}, \quad (\text{C.11})$$

where the correction factor $\gamma(t) \approx \gamma e^{-t/\tau_\mu}$ is small and decays at approximately the muon lifetime, we can recast the errors on the individual ratio sub-datasets as

$$\begin{aligned} \delta V(t)^2 &= \delta v_1(t)^2 \cdot \gamma(t) + \delta v_2(t)^2 \cdot \gamma(t) = (v_1(t) + v_2(t)) \cdot \gamma(t) = V(t) \cdot \gamma(t), \\ \delta U(t)^2 &= \delta u_+(t)^2 \cdot \gamma(t + T/2) + \delta u_-(t)^2 \cdot \gamma(t - T/2) \\ &\approx u_+(t) \cdot \gamma(t) e^{-T/2\tau} + u_-(t) \cdot \gamma(t) e^{+T/2\tau} \\ &\approx (u_+(t) + u_-(t)) \cdot \gamma(t) \cdot \left(1 + \frac{1}{2} \left(\frac{T}{2\tau}\right)^2\right) \\ &\approx U(t) \cdot \gamma(t), \end{aligned} \quad (\text{C.12})$$

where in the last step the $\frac{1}{2} \left(\frac{T}{2\tau}\right)^2$ term has been neglected because it's small. With these approximations having been made, the modified errors on the ratio points simply

become

$$\sigma_R^2 \rightarrow \sigma_R^2 \cdot \gamma(t), \quad (\text{C.13})$$

with the correction being the same as that on the pileup subtracted histogram. Credit to Reference [67] for this derivation.

Bibliography

- [1] P. Dirac. “The quantum theory of the electron”. In: *Proceedings of the Royal Society of London Series A, Containing Papers of a Mathematical and Physical Character* (1928).
- [2] J. E. Nafe, E. B. Nelson, and I. I. Rabi. “The Hyperfine Structure of Atomic Hydrogen and Deuterium”. In: *Phys. Rev.* 71 (12 June 1947), pp. 914–915. DOI: [10.1103/PhysRev.71.914](https://doi.org/10.1103/PhysRev.71.914). URL: <https://link.aps.org/doi/10.1103/PhysRev.71.914>.
- [3] Julian Schwinger. “On Quantum-Electrodynamics and the Magnetic Moment of the Electron”. In: *Phys. Rev.* 73 (4 Feb. 1948), pp. 416–417. DOI: [10.1103/PhysRev.73.416](https://doi.org/10.1103/PhysRev.73.416). URL: <https://link.aps.org/doi/10.1103/PhysRev.73.416>.
- [4] Joshua Ellis. “TikZ-Feynman: Feynman diagrams with TikZ”. In: *Comput. Phys. Commun.* 210 (2017), pp. 103–123. DOI: [10.1016/j.cpc.2016.08.019](https://doi.org/10.1016/j.cpc.2016.08.019). arXiv: [1601.05437 \[hep-ph\]](https://arxiv.org/abs/1601.05437).
- [5] Max Dohse. “TikZ-FeynHand: Basic User Guide”. In: (2018). arXiv: [1802.00689 \[cs.0H\]](https://arxiv.org/abs/1802.00689).
- [6] Tatsumi Aoyama et al. “Complete Tenth-Order QED Contribution to the Muon g-2”. In: *Phys. Rev. Lett.* 109 (2012), p. 111808. DOI: [10.1103/PhysRevLett.109.111808](https://doi.org/10.1103/PhysRevLett.109.111808). arXiv: [1205.5370 \[hep-ph\]](https://arxiv.org/abs/1205.5370).
- [7] Tatsumi Aoyama, Toichiro Kinoshita, and Makiko Nio. “Revised and Improved Value of the QED Tenth-Order Electron Anomalous Magnetic Moment”. In: *Phys. Rev.* D97.3 (2018), p. 036001. DOI: [10.1103/PhysRevD.97.036001](https://doi.org/10.1103/PhysRevD.97.036001). arXiv: [1712.06060 \[hep-ph\]](https://arxiv.org/abs/1712.06060).
- [8] C. Gnendiger, D. Stöckinger, and H. Stöckinger-Kim. “The electroweak contributions to $(g - 2)_\mu$ after the Higgs boson mass measurement”. In: *Phys. Rev.* D88 (2013), p. 053005. DOI: [10.1103/PhysRevD.88.053005](https://doi.org/10.1103/PhysRevD.88.053005). arXiv: [1306.5546 \[hep-ph\]](https://arxiv.org/abs/1306.5546).
- [9] Tadashi Ishikawa, Nobuya Nakazawa, and Yoshiaki Yasui. “Numerical calculation of the full two-loop electroweak corrections to muon $(g-2)$ ”. In: (2018). arXiv: [1810.13445 \[hep-ph\]](https://arxiv.org/abs/1810.13445).
- [10] F. Jegerlehner. *The Anomalous Magnetic Moment of the Muon*. Springer Tracts in Modern Physics. Springer Berlin Heidelberg, 2007. ISBN: 9783540726340. URL: <https://books.google.com/books?id=uxQj004Py6AC>.

- [11] D. Babusci et al. “Precision measurement of $\sigma(e^+e^- \rightarrow \pi^+\pi^-\gamma)/\sigma(e^+e^- \rightarrow \mu^+\mu^-\gamma)$ and determination of the $\pi^+\pi^-$ contribution to the muon anomaly with the KLOE detector”. In: *Phys. Lett.* B720 (2013), pp. 336–343. DOI: [10.1016/j.physletb.2013.02.029](https://doi.org/10.1016/j.physletb.2013.02.029). arXiv: [1212.4524 \[hep-ex\]](https://arxiv.org/abs/1212.4524).
- [12] T. Xiao et al. “Precision Measurement of the Hadronic Contribution to the Muon Anomalous Magnetic Moment”. In: *Phys. Rev.* D97.3 (2018), p. 032012. DOI: [10.1103/PhysRevD.97.032012](https://doi.org/10.1103/PhysRevD.97.032012). arXiv: [1712.04530 \[hep-ex\]](https://arxiv.org/abs/1712.04530).
- [13] Bogdan Malaescu. “Measurement of hadronic cross sections at BABAR with ISR and implications for the muon ($g-2$)”. In: *Proceedings, International Conference on the Structure and the Interactions of the Photon including the 20th International Workshop on Photon-Photon Collisions and the International Workshop on High Energy Photon Linear Colliders, PHOTON 2013: Paris, France, May 20-24, 2013*. 2014. arXiv: [1404.6887 \[hep-ex\]](https://arxiv.org/abs/1404.6887). URL: <http://www-public.slac.stanford.edu/sciDoc/docMeta.aspx?slacPubNumber=SLAC-PUB-16106>.
- [14] M. Ablikim et al. “Measurement of the $e^+e^- \rightarrow \pi^+\pi^-$ cross section between 600 and 900 MeV using initial state radiation”. In: *Phys. Lett.* B753 (2016), pp. 629–638. DOI: [10.1016/j.physletb.2015.11.043](https://doi.org/10.1016/j.physletb.2015.11.043). arXiv: [1507.08188 \[hep-ex\]](https://arxiv.org/abs/1507.08188).
- [15] Alexander Keshavarzi, Daisuke Nomura, and Thomas Teubner. “Muon $g-2$ and $\alpha(M_Z^2)$: a new data-based analysis”. In: *Phys. Rev.* D97.11 (2018), p. 114025. DOI: [10.1103/PhysRevD.97.114025](https://doi.org/10.1103/PhysRevD.97.114025). arXiv: [1802.02995 \[hep-ph\]](https://arxiv.org/abs/1802.02995).
- [16] Michel Davier et al. “Reevaluation of the hadronic vacuum polarisation contributions to the Standard Model predictions of the muon $g-2$ and $\alpha(m_Z^2)$ using newest hadronic cross-section data”. In: *Eur. Phys. J.* C77.12 (2017), p. 827. DOI: [10.1140/epjc/s10052-017-5161-6](https://doi.org/10.1140/epjc/s10052-017-5161-6). arXiv: [1706.09436 \[hep-ph\]](https://arxiv.org/abs/1706.09436).
- [17] T. Blum et al. “Calculation of the Hadronic Vacuum Polarization Contribution to the Muon Anomalous Magnetic Moment”. In: *Phys. Rev. Lett.* 121 (2 July 2018), p. 022003. DOI: [10.1103/PhysRevLett.121.022003](https://doi.org/10.1103/PhysRevLett.121.022003). URL: <https://link.aps.org/doi/10.1103/PhysRevLett.121.022003>.
- [18] Gilberto Colangelo et al. “Dispersive approach to hadronic light-by-light scattering”. In: *JHEP* 09 (2014), p. 091. DOI: [10.1007/JHEP09\(2014\)091](https://doi.org/10.1007/JHEP09(2014)091). arXiv: [1402.7081 \[hep-ph\]](https://arxiv.org/abs/1402.7081).
- [19] Gilberto Colangelo et al. “Dispersion relation for hadronic light-by-light scattering: theoretical foundations”. In: *JHEP* 09 (2015), p. 074. DOI: [10.1007/JHEP09\(2015\)074](https://doi.org/10.1007/JHEP09(2015)074). arXiv: [1506.01386 \[hep-ph\]](https://arxiv.org/abs/1506.01386).
- [20] Gilberto Colangelo et al. “Rescattering effects in the hadronic-light-by-light contribution to the anomalous magnetic moment of the muon”. In: *Phys. Rev. Lett.* 118.23 (2017), p. 232001. DOI: [10.1103/PhysRevLett.118.232001](https://doi.org/10.1103/PhysRevLett.118.232001). arXiv: [1701.06554 \[hep-ph\]](https://arxiv.org/abs/1701.06554).

- [21] Thomas Blum et al. “Lattice Calculation of Hadronic Light-by-Light Contribution to the Muon Anomalous Magnetic Moment”. In: *Phys. Rev.* D93.1 (2016), p. 014503. DOI: [10.1103/PhysRevD.93.014503](https://doi.org/10.1103/PhysRevD.93.014503). arXiv: [1510.07100 \[hep-lat\]](https://arxiv.org/abs/1510.07100).
- [22] Thomas Blum et al. “Connected and Leading Disconnected Hadronic Light-by-Light Contribution to the Muon Anomalous Magnetic Moment with a Physical Pion Mass”. In: *Phys. Rev. Lett.* 118.2 (2017), p. 022005. DOI: [10.1103/PhysRevLett.118.022005](https://doi.org/10.1103/PhysRevLett.118.022005). arXiv: [1610.04603 \[hep-lat\]](https://arxiv.org/abs/1610.04603).
- [23] Thomas Blum et al. “Using infinite volume, continuum QED and lattice QCD for the hadronic light-by-light contribution to the muon anomalous magnetic moment”. In: *Phys. Rev.* D96.3 (2017), p. 034515. DOI: [10.1103/PhysRevD.96.034515](https://doi.org/10.1103/PhysRevD.96.034515). arXiv: [1705.01067 \[hep-lat\]](https://arxiv.org/abs/1705.01067).
- [24] Nils Asmussen et al. “Hadronic light-by-light scattering in the anomalous magnetic moment of the muon”. In: *15th International Workshop on Tau Lepton Physics (TAU2018) Amsterdam, Netherlands, September 24-28, 2018*. 2018. arXiv: [1811.08320 \[hep-lat\]](https://arxiv.org/abs/1811.08320).
- [25] Andreas Nyffeler. “Precision of a data-driven estimate of hadronic light-by-light scattering in the muon $g - 2$: Pseudoscalar-pole contribution”. In: *Phys. Rev.* D94.5 (2016), p. 053006. DOI: [10.1103/PhysRevD.94.053006](https://doi.org/10.1103/PhysRevD.94.053006). arXiv: [1602.03398 \[hep-ph\]](https://arxiv.org/abs/1602.03398).
- [26] B. Lee Roberts. “The History of the Muon ($g - 2$) Experiments”. In: *15th International Workshop on Tau Lepton Physics (TAU2018) Amsterdam, Netherlands, September 24-28, 2018*. 2018. arXiv: [1811.06974 \[hep-ex\]](https://arxiv.org/abs/1811.06974).
- [27] G. W. Bennett et al. “Final Report of the Muon E821 Anomalous Magnetic Moment Measurement at BNL”. In: *Phys. Rev.* D73 (2006), p. 072003. DOI: [10.1103/PhysRevD.73.072003](https://doi.org/10.1103/PhysRevD.73.072003). arXiv: [hep-ex/0602035 \[hep-ex\]](https://arxiv.org/abs/hep-ex/0602035).
- [28] D. Hanneke, S. Fogwell, and G. Gabrielse. “New Measurement of the Electron Magnetic Moment and the Fine Structure Constant”. In: *Phys. Rev. Lett.* 100 (2008), p. 120801. DOI: [10.1103/PhysRevLett.100.120801](https://doi.org/10.1103/PhysRevLett.100.120801). arXiv: [0801.1134 \[physics.atom-ph\]](https://arxiv.org/abs/0801.1134).
- [29] Peter J. Mohr, David B. Newell, and Barry N. Taylor. “CODATA recommended values of the fundamental physical constants: 2014”. In: *Rev. Mod. Phys.* 88 (3 Sept. 2016), p. 035009. DOI: [10.1103/RevModPhys.88.035009](https://doi.org/10.1103/RevModPhys.88.035009). URL: <https://link.aps.org/doi/10.1103/RevModPhys.88.035009>.
- [30] Richard H. Parker et al. “Measurement of the fine-structure constant as a test of the Standard Model”. In: *Science* 360.6385 (2018), pp. 191–195. ISSN: 0036-8075. DOI: [10.1126/science.aap7706](https://doi.org/10.1126/science.aap7706). eprint: <https://science.sciencemag.org/content/360/6385/191.full.pdf>. URL: <https://science.sciencemag.org/content/360/6385/191>.
- [31] J. Jackson. *Classical Electrodynamics*. Wiley Indiana, 2011.

- [32] W. Liu et al. “High Precision Measurements of the Ground State Hyperfine Structure Interval of Muonium and of the Muon Magnetic Moment”. In: *Phys. Rev. Lett.* 82 (4 Jan. 1999), pp. 711–714. DOI: [10.1103/PhysRevLett.82.711](https://doi.org/10.1103/PhysRevLett.82.711). URL: <https://link.aps.org/doi/10.1103/PhysRevLett.82.711>.
- [33] E. D. Commins and P. H. Bucksbaum. *Weak interactions of leptons and quarks*. Cambridge University Press, 1983.
- [34] J. Grange et al. “Muon (g-2) Technical Design Report”. In: (2015). arXiv: [1501.06858 \[physics.ins-det\]](https://arxiv.org/abs/1501.06858).
- [35] Diktys Stratakis et al. “Accelerator performance analysis of the Fermilab Muon Campus”. In: *Phys. Rev. Accel. Beams* 20.11 (2017), p. 111003. DOI: [10.1103/PhysRevAccelBeams.20.111003](https://doi.org/10.1103/PhysRevAccelBeams.20.111003). arXiv: [1803.00597 \[physics.acc-ph\]](https://arxiv.org/abs/1803.00597).
- [36] Cary Yoshikawa et al. “Optimization of the Target Subsystem for the New g-2 Experiment”. In: (Jan. 2013).
- [37] A. Yamamoto et al. “The superconducting inflector for the BNL g-2 experiment”. In: *Nucl. Instrum. Meth.* A491 (2002), pp. 23–40. DOI: [10.1016/S0168-9002\(02\)01232-9](https://doi.org/10.1016/S0168-9002(02)01232-9).
- [38] Y. K. Semertzidis et al. “The Brookhaven muon (g-2) storage ring high voltage quadrupoles”. In: *Nucl. Instrum. Meth.* A503 (2003), pp. 458–484. DOI: [10.1016/S0168-9002\(03\)00999-9](https://doi.org/10.1016/S0168-9002(03)00999-9).
- [39] H. Wiedermann. *Particle Accelerator Physics*. Springer-Verlag New York, 1993.
- [40] M. J. Syphers. *Storage Ring Linear Tune Tables*. Muon g-2 DocDB 11547. 2018.
- [41] K. Khaw. *How each dataset is different for Run 1 of E989*. Muon g-2 DocDB 15781. 2019.
- [42] H. Binney. *T0: update and current work*. Muon g-2 DocDB 10162. 2018.
- [43] A. Fienberg. *T0 Detector*. Muon g-2 DocDB 10911. 2018.
- [44] P. Kammel et al. *Inflector Beam Monitoring System Justification Document*. Muon g-2 DocDB 2722. 2015.
- [45] B. MacCoy and P. Kammel. *IBMS Update*. Muon g-2 DocDB 10944. 2018.
- [46] F. Gray. *Fiber Harp Beam Monitor*. Muon g-2 DocDB 8366. 2017.
- [47] A. T. Fienberg et al. “Studies of an array of PbF₂ Cherenkov crystals with large-area SiPM readout”. In: *Nucl. Instrum. Meth.* A783 (2015), pp. 12–21. DOI: [10.1016/j.nima.2015.02.028](https://doi.org/10.1016/j.nima.2015.02.028). arXiv: [1412.5525 \[physics.ins-det\]](https://arxiv.org/abs/1412.5525).
- [48] J. Kaspar et al. “Design and performance of SiPM-based readout of PbF₂ crystals for high-rate, precision timing applications”. In: *JINST* 12.01 (2017), P01009. DOI: [10.1088/1748-0221/12/01/P01009](https://doi.org/10.1088/1748-0221/12/01/P01009). arXiv: [1611.03180 \[physics.ins-det\]](https://arxiv.org/abs/1611.03180).

- [49] David A. Sweigart. “A new MicroTCA-based waveform digitizer for the Muon g-2 experiment”. In: *PoS ICHEP2016* (2016), p. 845. DOI: [10.22323/1.282.0845](https://doi.org/10.22323/1.282.0845). arXiv: [1612.05145 \[physics.ins-det\]](https://arxiv.org/abs/1612.05145).
- [50] A. Anastasi et al. “The laser control of the muon $g - 2$ experiment at Fermilab”. In: *JINST* 13.02 (2018), T02009. DOI: [10.1088/1748-0221/13/02/T02009](https://doi.org/10.1088/1748-0221/13/02/T02009).
- [51] S. Charity. “Beam profile measurements using the straw tracking detectors at the Fermilab muon $g - 2$ experiment, and a study of their sensitivity to a muon electric dipole moment”. PhD thesis. University of Liverpool, 2018.
- [52] W. Riegler W. Blum and L. Rolandi. *Particle Detection with Drift Chambers*. Springer-Verlag Berlin Heidelberg, 2008.
- [53] W. Turner. “The construction and commissioning of the straw tracking detector in the new muon $g - 2$ experiment at Fermilab”. PhD thesis. University of Liverpool, 2018.
- [54] C. Green et al. “The Art Framework”. In: *J. Phys. Conf. Ser.* 396 (2012), p. 022020. DOI: [10.1088/1742-6596/396/2/022020](https://doi.org/10.1088/1742-6596/396/2/022020).
- [55] T. Walton. *Track Finding Overview*. Muon g-2 DocDB 7580. 2017.
- [56] T. Walton and J. Price. *Track formation details*. Muon g-2 DocDB 8555. 2017.
- [57] J. Price. *Track Finding - simple pattern recognition*. Muon g-2 DocDB 5793. 2017.
- [58] V. Innocente, M. Maire, and E. Nagy. “GEANE: Average tracking and error propagation package”. In: *MC 91: Detector and event simulation in high-energy physics. Proceedings, Workshop, Amsterdam, Netherlands, April 8-12, 1991*. 1991, pp. 58–78. URL: http://innocentonnice.web.cern.ch/innocentonnice/napoli99/geane_manual.ps.
- [59] Lia Lavezzi. “The fit of nuclear tracks in high precision spectroscopy experiments”. pp. 57-86. PhD thesis. Pavia U., 2007. URL: http://bamboo.pv.infn.it/doc/L_Lavezzi.pdf.
- [60] K. Lassila-Perini and L. Urban. “Energy loss in thin layers in GEANT”. In: *Nucl. Instrum. Meth.* A362 (1995), pp. 416–422. DOI: [10.1016/0168-9002\(95\)00344-4](https://doi.org/10.1016/0168-9002(95)00344-4).
- [61] A. Strandlie and W. Wittek. “Derivation of Jacobians for the propagation of covariance matrices of track parameters in homogeneous magnetic fields”. In: *Nucl. Instrum. Meth.* A566 (2006), pp. 687–698.
- [62] V. Innocente and E. Nagy. “Trajectory fit in presence of dense materials”. In: *Nucl. Instrum. Meth.* A324 (1993), pp. 297–306. DOI: [10.1016/0168-9002\(93\)90992-Q](https://doi.org/10.1016/0168-9002(93)90992-Q).
- [63] J. Price and S. Charity. *Extrapolation uncertainty*. Muon g-2 DocDB 14920. 2018.

- [64] A. Fienberg. “Measuring the Precession Frequency in the E989 Muon $g - 2$ Experiment”. PhD thesis. University of Washington, 2019.
- [65] M. Schwartz. *Quantum Field Theory and the Standard Model*. Cambridge University Press, 2014.
- [66] F. Farley et al. *Estimation of Error in Differential Pileup Subtracted Data*. E821 Muon g-2 Note 377. 2018.
- [67] J. Paley. “Measurement of the Anomalous Magnetic Moment of the Negative Muon to 0.7 Parts Per Million”. PhD thesis. Boston University, 2004.

Nicholas Kinnaird

512-922-0534 | nickkinn@bu.edu | 205 N Oakhurst Dr, Aurora, IL

6.2 Education

Boston University
Ph.D. in Physics

Boston, MA
2019

Dissertation: Measurement of the Magnetic Anomaly of the Muon to X parts per billion
in Run 1 of the Fermilab Muon $g - 2$ Experiment

Boston University
M.A. in Physics

Boston, MA
2016

University of Texas at Austin
B.S. in Physics

Austin, TX
2013

University of Texas at Austin
B.S. in Mathematics

Austin, TX
2013